Aerodynamic interaction of a boundary layer ingesting propeller with a fuselage aft-cone

Martijn van Sluis [*] , Tomas Sinnige [†] and Leo L.M. Veldhuis [‡]
Delft University of Technology, Delft, Zuid-Holland, 2628 CD, The Netherlands

For the next generation of transport aircraft, Boundary Layer Ingestion (BLI) is being proposed as a promising technology, to reduce energy consumption. However, the aerodynamic interaction between the propulsor and the fuselage boundary layer has received little attention. In this study, an experimental approach is used to study the effect of a fuselage aft-cone mounted propeller on the flow around a fuselage aft-body. An idealized fuselage model with integrated rear propeller is tested in a low-subsonic wind-tunnel. The loads on the propeller were measured directly with the use of a rotating shaft balance. Integration of the aft-fuselage pressure field allowed for a complete force decomposition. Operation of the propeller was shown to significantly increase pressure and friction drag on the fuselage. Furthermore, hotwire measurements show that the turbulence characteristics of the fuselage boundary layer upstream of the propeller were altered by the propeller. Compared to the propeller off measurement, a clear deviation from the universal log-law was observed. Phase-locked hotwire and embedded microphone data reveal small in-phase fluctuations with the propeller blade passage. Despite their persistence throughout the boundary layer, the fluctuations are not believed to significantly impact the mean inflow to the propeller or affect its performance. Despite their insignificant impact on propeller performance, the fluctuations could still be relevant in terms of noise and vibrations.

Nomenclature

Latin symbols

c	Chord length, m	C_T	Thrust coefficient, $T/(\rho n^2 D_p^4)$
C_D	Drag coefficient, $D/(0.5\rho U_\infty^2 S)$	C_Y	Side force coefficient, $F_y/(\rho n^2 D_p^4)$
C_Q	Torque coefficient, $Q/(\rho n^2 D_p^5)$	D	Drag force, N
		D_p	Propeller diameter, m

[*]PhD candidate, Flight Performance and Propulsion, Delft University of Technology, M.vansluis@tudelft.nl
[†]Assistant professor, Flight Performance and Propulsion, T.Sinnige@tudelft.nl
[‡]Full Professor, Flight Performance and Propulsion, L.L.M.Veldhuis@tudelft.nl

f	Frequency, Hz
H	Boundary layer shape factor
I_x	Turbulence Intensity, $u^{'}/U_\infty$
J	Advance ratio, $U_\infty/(n \cdot D_p)$
K	Acceleration parameter, $\nu/u^2 dU/dx$
L	Fuselage length, m
M	Mach number
n	Propeller rotational speed, $1/s$
p	Static pressure, Pa
p_t	Total pressure, Pa
R	Propeller radius, m
Re	Reynolds number
S	Fuselage cross-section area, m^2
Str	Strouhal number, $D_p f/u$
T_C	Thrust coefficient, $T/(q_\infty \pi/4 D_p^2)$
u^+	Shear stress velocity, $\sqrt{\tau_w/\rho}$
u, v, w	Cartesian velocity components, m/s
y^+	Nondimensional wall distance, $u^+ y/u$
x, y, z	Cartesian coordinates

Greek symbols

β	Angle of side-slip, deg
$\beta_{0.70R}$	Propeller pitch angle at $0.70R$, deg
δ_{99}	Boundary layer thickness, m
η	Efficiency, $(C_T \cdot J)/C_P$
ρ	Air density, kg/m^3
τ_w	Shear stress, Pa
Θ	Momentum loss thickness, m
ϕ	Azimuthal position aft-body, deg

Subscripts

aft	aft-body of fuselage
iso	isolated (fuselage)
spin	spinner and hub assembly
fric	friction (drag)
pres	pressure (drag)

Acronyms

BLDC	Brush-Less Direct Current
BLI	Boundary Layer Ingestion
BPF	Blade Passing Frequency
CTA	Constant Temperature Anemometry
ESC	Electronic Speed Controller
ESDU	Engineering Science and Data Unit
FSR	Fuselage Slenderness Ratio
LTT	Low Turbulence Tunnel
PSD	Power Spectral Density
RANS	Reynolds Averaged Navier-Stokes
RMS	Root Mean Square
RSB	Rotating Shaft Balance
SPL	Sound Pressure Level
ZPG	Zero Pressure Gradient

I. Introduction

To keep civil aviation viable, ambitious goals regarding emissions and noise have been set by the Advisory Council for Aeronautics Research in Europe (ACARE) [1]. These goals, as part of the Strategic Research and Innovation Agenda (SRIA) [2], aim at reducing the emission of CO_2 per passenger kilometre by 60% in 2035 relative to the year 2000. On top of this, the exponential growth that aviation has experienced over the past decades, is expected to continue [3]. Currently, aviation is responsible for 2% of all greenhouse gas emissions [4] and without intervention this will more than double by 2050 [5]. New technological developments with the potential to enter service within the next decade are urgently required. One such technology is Boundary Layer Ingestion (BLI). Due to synergy of the integrated propulsion systems with the airframe, fuel savings can be achieved [6][7][8][9]. Different BLI designs have been explored, but ingestion of the entire fuselage boundary by a single aft-mounted propulsor has been shown to be able to provide the largest fuel saving benefit [10].

However, the close coupling between the airframe and the propulsor introduces challenges. A mutual interaction between the upstream flow field and the propulsor loading exists. Examples of aerodynamic interactions for a tailcone-mounted propeller BLI configuration are shown in Figure 1. As such, the classical distinction of aerodynamic forces into drag and thrust becomes ambiguous, since elements of the main body (i.e. fuselage) are part of the streamtube leading into and out of the propulsor. [11] Different drag-thrust bookkeeping and analysis schemes have been proposed to solve this ambiguity [12][13]. Although these bookkeeping schemes provide good insight into the exchange of energy and momentum between the main body and the propulsor, their application is not straightforward.

Furthermore, operating a fan or propeller in a turbulent and nonuniform flow is known to increase both tonal and broadband noise [14][15]. Nevertheless, the majority of studies into BLI concepts have been performed using time-averaged solution methods. On top of this, there is often no direct coupling between the inflow and the propulsor [6][8]. Hence, any unsteady aerodynamic interaction between the relatively thick fuselage boundary layer and the propulsor is

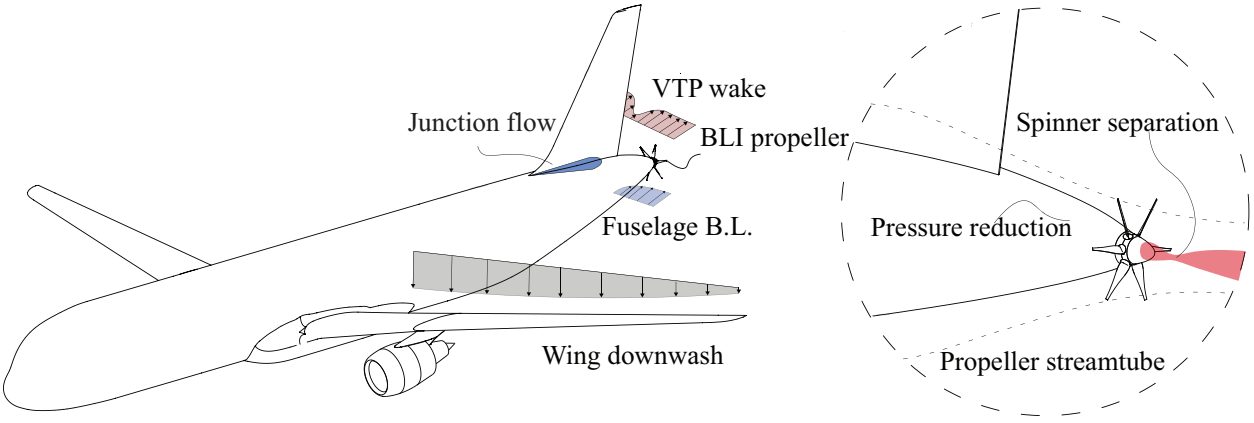

Fig. 1 Schematic with examples of aerodynamic interferences between a boundary layer ingesting propeller and the airframe. Horizontal stabilizer not shown.

not taken into account. More elementary aerodynamic studies provide insight into aerodynamic interactions that could be relevant for BLI configuration. For example, it is demonstrated that an axisymmetric boundary layer subjected to an unsteady pressure gradient undergoes a transient response and changes its main characteristics [16]. Furthermore, it is found that unsteady pressure gradients can affect the stability of the friction sub-layer [17]. Additionally, subjecting a boundary layer to a strong favourable pressure gradient changes the turbulent characteristics of the boundary layer significantly [18]. However, it is not clear if these unsteady interactions would occur at the pressure gradients and Strouhal number representative of a fuselage aft-cone BLI configuration.

Other possible interactions, as depicted in Figure 1, are not unique to a fuselage aft-cone mounted propeller BLI configuration and have recieved prior study. For example, the aerodynamic and aero-acoustic interaction of a pusher propeller and upstream lifting surface [14][19][20][21] has been well documented. Similarly, the ingestion of a vortex (e.g. junction horse-shoe vortex) has recieved prior attention and shown to enhance the thrust and noise characteristics, strongly depending on the relative radial position of the vortex impingement. [22][23][24]

Therefore, this paper aims to investigate the aerodynamic interaction between an aft-cone mounted propeller and the airframe. Specifically, this paper aims to study if there is a direct time-dependent coupling of the propeller with the fuselage boundary layer. To avoid the influence of model assumptions (e.g. two equation eddy viscosity turbulence models) on the boundary layer prediction or very large numerical grids (e.g. LES), an experimental approach is selected. Subsonic wind tunnel tests with a wind-tunnel model including an idealized fuselage aft-cone mounted propeller are performed, to measure the upstream influence of the propeller. To associate the occurring aerodynamic interactions to the propeller performance, the loads on the propeller are measured directly with a rotating shaft balance. Although the thrust and torque for a BLI propeller configuration have been measured before [25], to the authors knowledge, this is the first study into BLI with a fully integrated setup and that measures all force components. The integrated measurement of the forces allows for a direct evaluation of the aerodynamic forces with thrust-drag bookkeeping as used in conventional aircraft designs. The outcome of this study will contribute to a better comprehension of the fuselage-propulsor interaction for non-ducted BLI configurations.

II. Experimental setup

The primary objective of this work is to investigate the relative change in fuselage boundary layer characteristics, as a direct result of propeller action. The focus is to identify and characterize the specific interactions that may occur and to provide a reference for future study. An exact geometric representation of a conventional fuselage for a transport aircraft and measurement of its aerodynamic performance is not part of the objective. Therefore, subsonic wind tunnel tests were performed with an axisymmetric fuselage model and a reference propeller. Wind-tunnel corrections have not been applied, as the objective is not to quantify absolute performance but rather to investigate changes in aerodynamic characteristics with propeller operation. A description of the wind-tunnel setup and model is presented in this section.

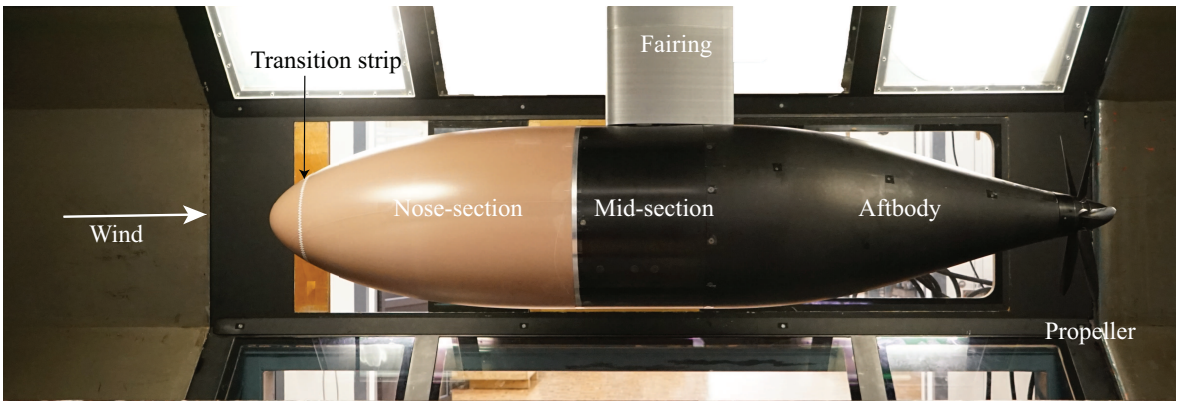

Fig. 2 Photograph of the model installed in the test section of the Low Turbulence Tunnel (LTT).

A. Aerodynamic scaling and similarity parameters

The above rationale of focussing on relative changes in aerodynamic properties compared to the baseline configuration (no propeller) is further strengthened by the fact that the primary aerodynamic scaling parameters cannot be matched with the full-scale aircraft during low-speed wind tunnel testing. The length-based Reynolds number of the model fuselage boundary layer is $Re_L \approx 7.50e^6$ and the maximum Mach number during testing was $M = 0.175$. As a reference, at full-scale cruise conditions, Re and M would be around $200e^6$ and 0.78, respectively. The Reynolds number has a direct effect on the characteristics of the fuselage boundary layer, such as the transition location and relative thickness. In order to limit the effect of reduced Reynolds number, the fuselage length is maximized within the geometrical constraints of the wind-tunnel facility. Furthermore, the boundary layer is forced to transition at the nose to guarantee the development of a fully-turbulent boundary layer over the body. Next to the scaling of friction and inertial forces, the effect of compressibility of air cannot be simulated in a low-speed wind-tunnel. For reference, the tip Mach number of the propeller at $J = 1.05$ is equal to $M_{tip} = 0.53$. Although the conditions of cruise flight cannot be replicated, the flow parameters in the wind-tunnel resemble typical takeoff conditions.

B. Wind-tunnel facility

The wind-tunnel experiments were performed at the Low Turbulence Tunnel (LTT) of Delft University of Technology. The LTT is an atmospheric wind tunnel and has a closed-loop, closed test-section design. The test section has a length of 2.60 m and an octagonal cross section with a width of 1.80 m and height of 1.25 m. The measurements were performed at a fixed tunnel velocity of $U_\infty = 60$ m/s with a free-stream turbulence intensity below 0.03% [26]. In the case of propeller performance measurements, it was chosen to keep the Mach number constant at $M = 0.175$.

C. Fuselage model

A photograph of the model, installed in the test-section, is shown in Figure 2. An overview of the model together with its main dimensions is presented in Figure 3. To reduce the complexity of the flowfield, an axisymmetric fuselage shape

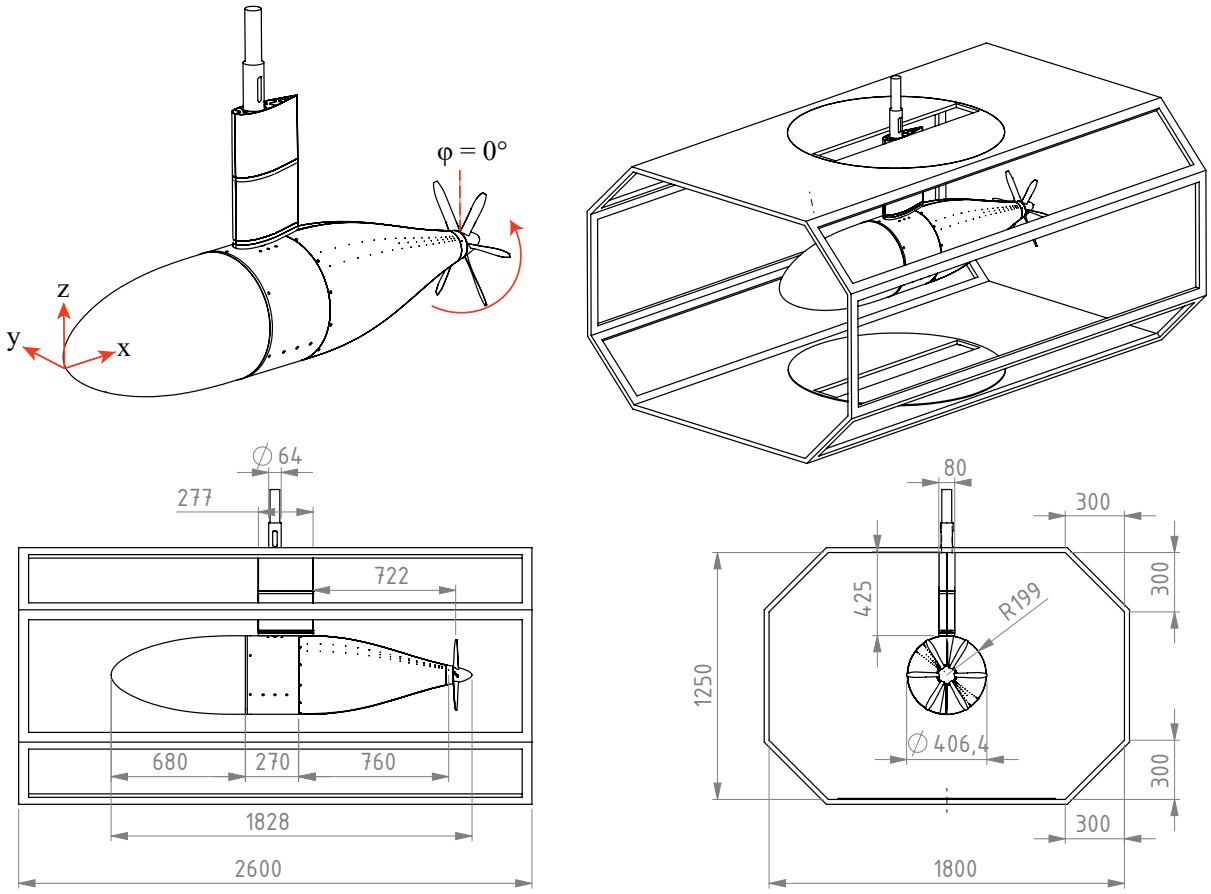

Fig. 3 Drawing of the model installed in the wind tunnel test-section, including fairing and model support beam. All dimensions are shown in mm.

is adopted. Nonaxisymmetric effects, such as the impact of aft-fuselage upsweep, are beyond the scope of this study. In order to minimize the effect of model support interference on the flow field over the aft fuselage [27], the model radius is maximized. Although this results in a model with a low Fuselage Slenderness Ratio ($L_{fus}/D_{fus} \approx 4.5$) and increased solid blockage, it should ensure that the assumption of axisymmetric flow can be maintained for the majority of the circumference. The model features a nose representative of a conventional passenger transport aircraft and is shaped according to guidelines by the Engineering Science Data Unit (ESDU) [28]. The nose has an overall length of 680 mm. The curvature of the axisymmetric aftbody, up to the propeller hub, is designed according to ESDU II [28]. The length of the aftbody is 760 mm and a curvature constant $k_1 = 1.77$ is selected. A cylindrical midsection of 270 mm length and 198 mm radius represents the midsection of the fuselage. The overall length of the model, including the propeller hub and spinner, amounts to 1828 mm. The nose section is constructed from a solid block of polyurethane (Raku-Tool® MB-0600). A sealant has been applied to guarantee a smooth and non-porous surface finish. The midsection and aftbody shells are constructed out of aluminium. The shells for the aftbody are designed such that the aftbody can rotate

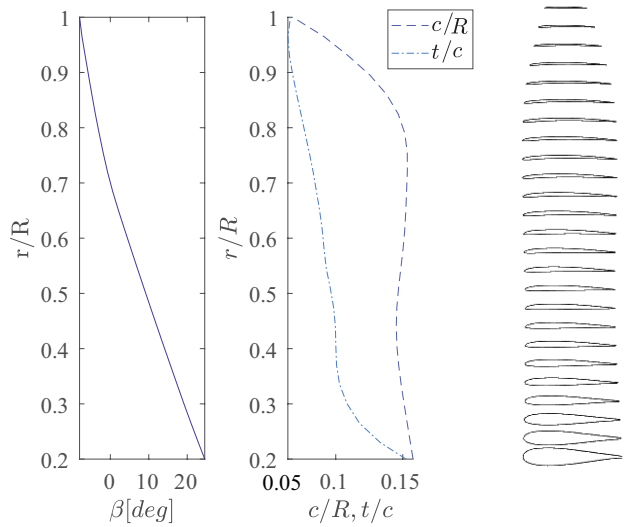

Fig. 4 Description of the XPROP blade geometry at $\beta_{0.7R} = 0\,\mathrm{deg}$ (left) and blade representation with untwisted blade geometry and airfoils (right).

around the longitudinal axis and such that measurements of time-averaged and unsteady pressure can be taken over the entire circumference with a limited number of sensors. This is discussed in more detail in Section II.D.

The model is suspended by a central cylindrical beam to an external six-component mechanical balance. The beam is shielded to the flow by means of an aerodynamic fairing, mounted directly to the roof of the test section. The gap between the fairing and the fuselage model is kept minimal and is less than 0.2mm at the leading edge and about 1 mm at the trailing edge. The model is rotated around the beam central axis to model the effect of non-zero angle of sideslip. It is ensured that the fairing does not contact either the model or the beam, to avoid disruption of the force balance measurements. The fairing does not co-rotate with the model and remains at zero incidence angle with the freestream. To minimize the disturbance of the flow behind the fairing, an airfoil designed for low Reynolds number and minimal wake is desired. A McMasters-Henderson [29] airfoil profile with a thickness-to-chord ratio $t/c = 0.18$ was selected. No taper or sweep is applied to the fairing. Considering the constraints set by beam diameter, the constant chord length was selected to be $c = 270$ mm to limit the thickness-to-chord ratio ($t/c = 0.18$). Higher values of t/c would results in a larger fairing wake. A zig-zag tape of 0.225 mm thickness and 12 mm width was placed at the nose ($x/L = 0.05$) to ensure a fixed transition location. Transition of the boundary layer was checked for all operation conditions during the experiment, with the use of a microphone stethoscope. Although it is known that zig-zag transition strips, compared to carborundum strips, can introduce additional vorticity in the boundary layer and, therefore, alter the turbulent characteristics, it has been demonstrated that sufficiently downstream this effect can be neglected [30].

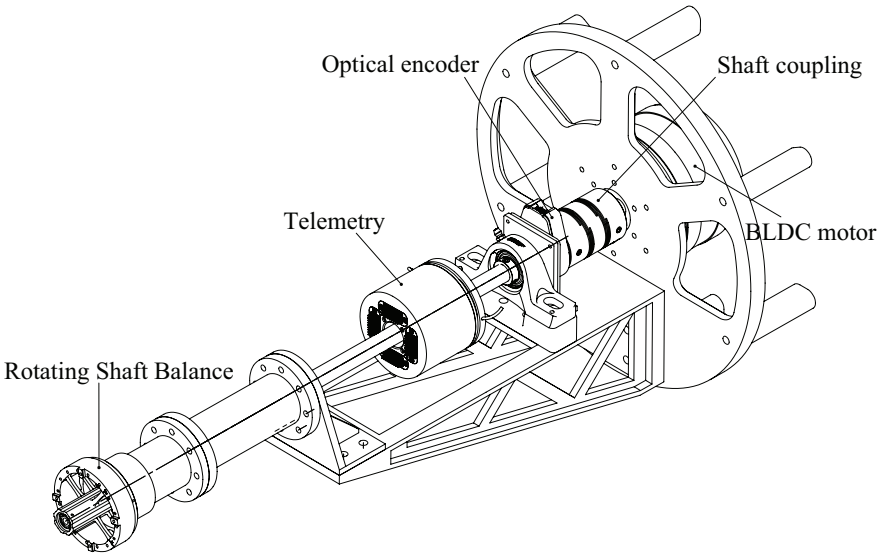

Fig. 5 Drawing of the power train with indication of the main components.

Propeller

In order to compare the installed propeller performance, an existing reference propeller has been selected (TUD-XPROP) [31] [32]. The blade characteristics of the propeller are presented in Figure 4. The propeller has a diameter of $D_p = 0.4064$ m and a maximum rotational speed of 10000 rpm. Although the propeller is representative of a conventional turboprop and designed for uniform inflow, the operation conditions are selected ($\beta_{0.70R} = 30°$) such that the sectional inflow angles are still within range of the design values. Note that the propeller blades are only partially submerged in the fuselage boundary layer, since the propeller size is approximately equal to the fuselage diameter. To be able to compare the propeller on and propeller off cases, the propeller blades can be substituted with bare blade feet to retrieve a propeller off (referred to as isolated fuselage) configuration.

Powertrain

The power train, shown in Figure 5, is suspended to the main cylindrical section of the model. In this way, the transfer of heat and vibrations of the powertain to the aft-fuselage shells is kept to a minimum. Furthermore, it enables the shells of the aftbody to rotate independently around the model main axis. The core of the powertain consists of a brushless DC inrunner electric motor with liquid cooling (Plettenberg Nova 15-50-B4 S P30). The maximum mechanical output amounts to 15 kW peak power and 16 Nm of torque. At peak performance, the motor efficiency is $\eta = 0.89$. To allow for extended measurements at high power settings, a 2.5 kW heat-capacity external water chiller is employed. Peak temperatures of the electric motor during testing remained always below 40° C. Electric power to the motor is supplied by a 15 kW bi-directional power supply (Delta Elektronika SM15K) and controlled via an MGM Compro (HBC 280120) ESC. The motor is connected to a 640 mm long hollow, steel shaft through a flexible shaft coupling (NBK MST-50). In

total, the shaft is supported by four different high-performance bearings to restrain the shaft movement. A US Digital E6 (1024 CPR) differential optical encoder is used to precisely measure the rotational speed. The assembly of shaft, hub, propeller and RSB have been balanced according to DIN ISO 21940-11 class G2.5.

D. Measurement Techniques

1. Forces and moments

The integral aerodynamic forces and moments acting on the model are measured by a six-component mechanical balance. With an error of less than 0.02 N ($\epsilon < 0.15\%\ C_{D,iso}$) over the entire measurement range, consistently accurate drag measurements can be obtained regardless of the force magnitude. Since the fairing shields the beam connecting the model to the balance from the flow, the resultant aerodynamic force represents the net vehicle force. To distinguish the propeller thrust separately from the vehicle drag, a custom six-component Rotating Shaft Balance (RSB) is used. The design is based on eight strain-gauge equipped flexures. Two NTC temperature sensors are placed on the inner and outer ring for temperature calibration. In combination with the TUD-XPROP, the uncertainty in the force measurements is established to be below 0.5% FS. To transmit the RSB data signals and supply power, a digital custom 24-channel telemetry system (MANNER Sensortelemetrie GmbH) is used. The bandwidth for each channel is up to 5 kHz and the total sample rate amounts to 12 kS/s. Before and after each propeller performance measurement, the propeller assembly was aligned with a reference position to exclude the influence of static force differences on the tare measurements for the in-plane components. A measurement time of $t = 10$ s was used for force measurements.

2. Static pressure ports

To map changes in the pressure field over the aftbody, each shell was equipped with two streamwise rows of 16 pressure taps. The taps were distributed using a cosine spacing, with the smallest spacing towards the propeller hub. The locations are presented in Table 1. The azimuthal angle between the two rows is 15°. The aftbody can be rotated with discrete steps of 30°, which yields a resolution of the pressure measurements in azimuthal direction of 15°. The pressure ports were connected to PSI Pressure Systems ESP-64HD and ESP-32HD pressure scanner on channels with a range up to 1 psi. The pressure scanners are connected to a PSI DTC Initium data acquisition system. The stated accuracy of the pressure scanner is ±0.05 FS, meaning a ±4 Pa uncertainty in the aft-body pressure measurements. The pressure data are sampled at a rate of 50 Hz. In addition, the measurement time for pressure measurements was $t = 10$ s.

3. Microphones

In addition to the measurement of the time-averaged pressure over the aftbody, microphones were used to capture the pressure fluctuations. The microphones were placed in a single streamwise row on the left aftbody shell. To avoid possible interference with the static pressure ports, the row is located at an angular offset of 37.5° relative to the second

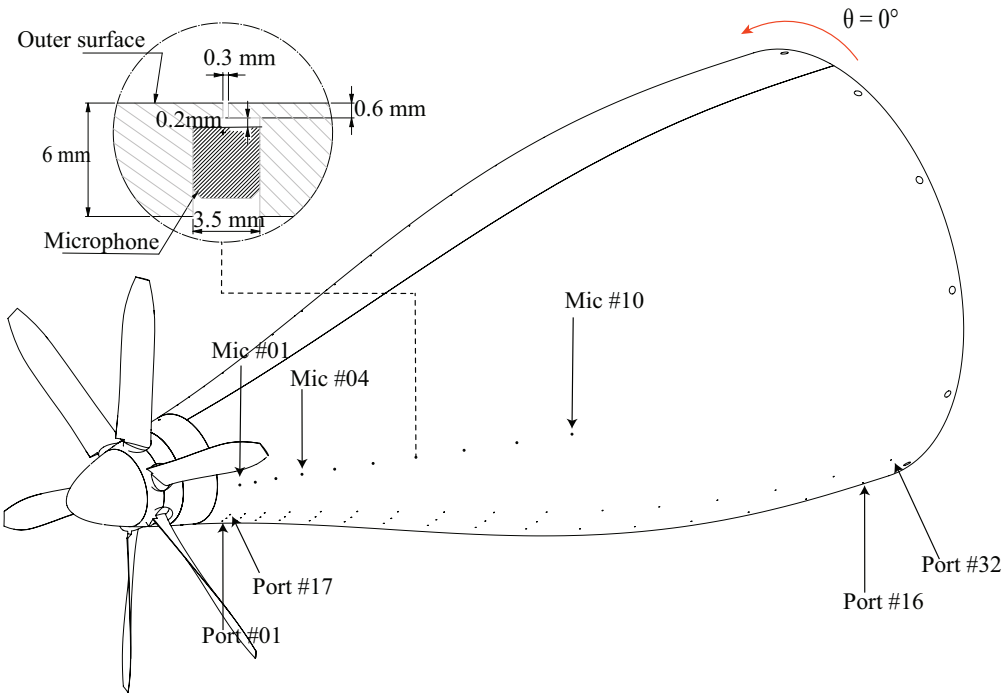

Fig. 6 Drawing the aftbody with the microphone and pressure ports.

row of pressure taps. In total, 10 microphones are recessed from the surface in individual pockets behind a 0.3 mm pinhole (Figure 6). Their axial location coincides with the location of th corresponding pressure taps $1-10$, as shown in Table 1. The microphones (MM Audio MM-PSM-L) can measure in the range of 20 Hz - 20 kHz and have a maximum input level of 150 dB at 1 kHz together with an equivalent noise floor of 32dBA. The Blade Passing Frequency (BPF) varied between 738 Hz and 844 Hz. As such, the microphones should be able to measure up to the 24th harmonic of the BPF. The resonance frequency of the cavities are calculated 16.8 kHz. A sampling rate of 51.2 kHz was used, with 15 s of acquisition time per data point. The microphones were frequency-dependently calibrated using a LinearX M53 reference microphone in combination with a GRAS 42AA piston phone. The microphones were connected to a custom

Table 1 Overview of the microphone and pressure tap axial locations. Propeller pitch axis at $x/L_{fus} = 0.9535$.

No.	1	2	3	4	5	6	7	8
x/L_f	0.9169	0.9087	0.8978	0.8841	0.8671	0.8474	0.8255	0.8009
Mic	•	•	•	•	•	•	•	•
Tap	•	•	•	•	•	•	•	•
No.	9	10	11	12	13	14	15	16
x/L_f	0.7741	0.7457	0.7150	0.6833	0.6499	0.6155	0.5799	0.5438
Mic	•	•						
Tap	•	•	•	•	•	•	•	•

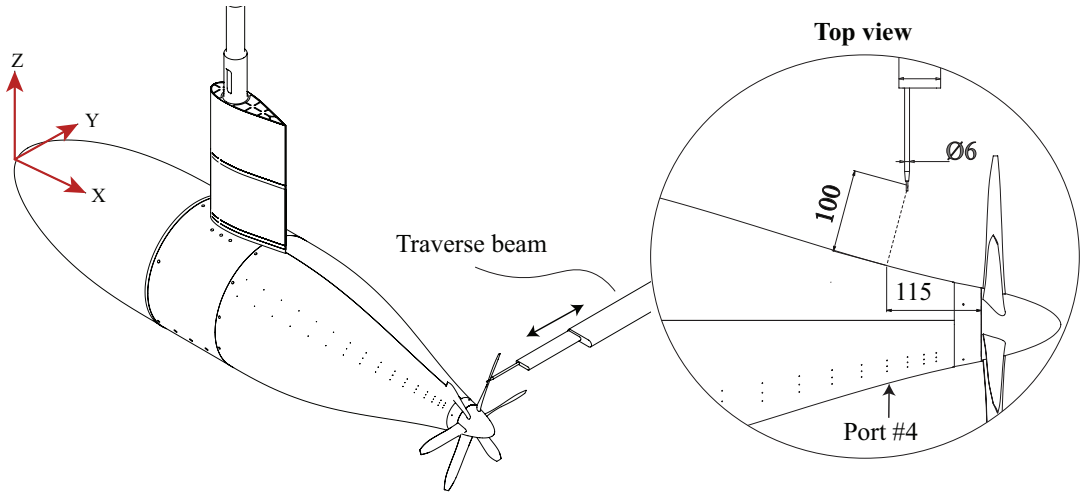

Fig. 7 Illustration of the probe support strut and traverse direction for boundary layer measurements. All dimensions in mm.

circuitry board and powered by a low-noise linear DC power supply. The microphone signals were acquired by an array of National Instruments NI-9234 DAQ modules mounted inside the model. The data was recorded synchronously with the 1-per-revolution ($1p$) trigger signal of the optical encoder, to allow for propeller phase-locked processing of the data.

4. Boundary layer measurements

In order to study the boundary layer ahead of the propeller, velocity and pressure measurements were taken along a trajectory perpendicular to the local surface inclination, coinciding with the 4th microphone location ($x/L_{fus} = 0.8840$). An illustration of the procedure is presented in Figure 7. The boundary layer measurements are performed in the horizontal plane using a support beam mounted on an external traverse system. Each measurement was started 100 mm away from the surface and consisted of 100 measurement points. A double cosine spacing was selected to increase the resolution near the surface. The pitch axis of propeller is located at $x/L_{fus} = 0.9535$, hence the boundary layer was measured $0.3233D_p$ upstream of the propeller. Measurements closer to the propeller were not possible to avoid intersection of the probe support sting with the propeller blades.

Sampling of the pressure throughout the boundary layer was conducted using a pitot-static tube. The pitot-static tube was given an in-plane inclination with respect to the free stream velocity of 10° to align it better with the local flow direction. Note that the local surface tangent is inclined by 14° with respect to the longitudinal axis. Depending on the angle of the local streamlines, the pitot-static tube was at a non-zero incidence angle with the local incoming flow. No correction was applied to mitigate any measurement error, as the true local flow angle is not known. The pitot-static tube was connected to the pressure scanner at a 0.36 psi port, with a rated uncertainty of ±1.5 Pa.

To obtain the velocity profile of the boundary layer, measurements using Constant Temperature Anemometry (CTA) were performed. A single-wire miniature 90° perpendicular probe (Dantex 55P14) was used. In contrast to the pitot-static

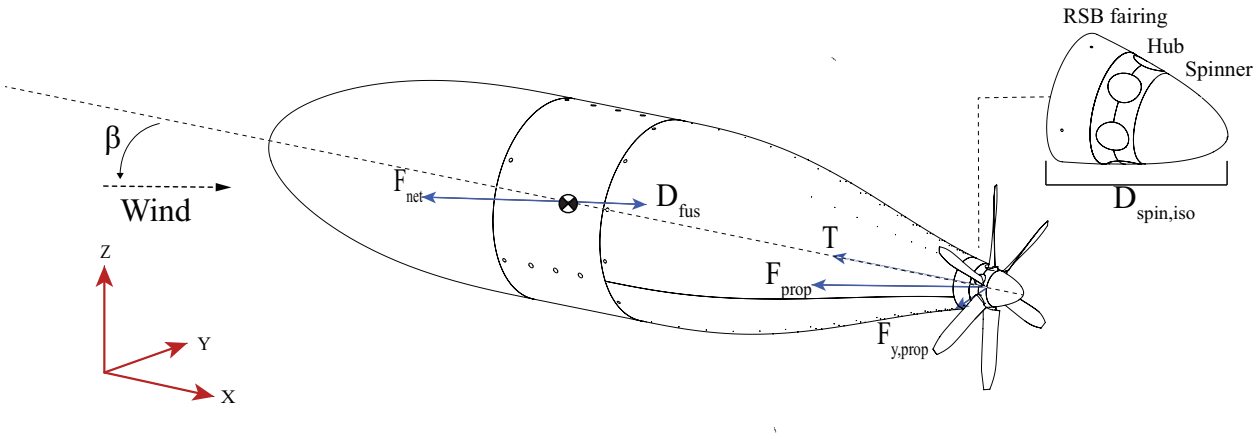

Fig. 8 Decomposition of the forces acting on the model.

measurements, the probe was not inclined with the local surface curvature. The probe was traversed at a near-identical trajectory as the pitot-static probe, only adjusted to approach the wall as close as possible. Due to small displacements of the aftbody and limited optical excess, a safety margin of the probe distance to the wall of 0.3 mm was maintained. Given the fact that the aftbody is constructed from black anodized aluminium, the conduction of heat from the probe in close proximity to the wall is expected to influence the measurement. This wall-effect is known to occur, in wind-off conditions, at distances below 0.5 mm. [33] The zero position at the wall was determined by using a contact sensor created from a defective identical probe and a multimeter. The hotwire was connected to an IFA 300 STD Bridge. Before each measurement run, a new calibration was performed to account for temperature effects (e.g. heating up of the wind-tunnel). During the calibration, the probe was aligned with a wall-mounted pitot-static tube connected to a Mensor (Model 2101) digital pressure scanner. The model version used had a measurement range up to 0.5 psig and a rated accuracy of 0.01% FS. The sampling frequency was set to 51.2 kHz.

III. Results

The results are divided into two parts. First, the time-averaged effects of the propeller on the fuselage aft-cone are discussed in subsection III.A. Once the changes to the mean flow field are explained, the unsteady interactions are discussed in subsection III.B.

A. Effect of propeller installation on fuselage drag

In this section, the mean aerodynamic effects of a boundary layer ingesting propeller on the flow over the fuselage aft-cone are discussed. Two main time-averaged interactions to the upstream flow field can be expected: a decrease in the upstream pressure due to induction by the propeller and an increase in velocity as a result of streamtube contraction. Together, these two interactions yield the additional drag due to propeller installation.

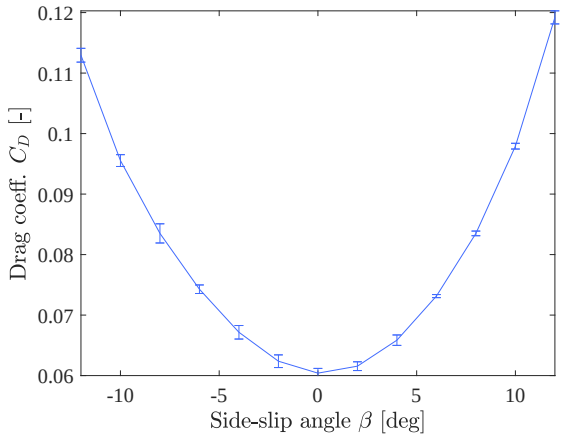

Fig. 9 Drag-polar of the isolated fuselage $Re_L = 7.24e^6$.

$$\Delta D_{ins} = D_{fus,prop} - D_{fus,iso} = F_{net} - F_{prop} - (D_{fus,iso} - D_{spin,iso}) \tag{1}$$

, where F_{net} is the net vehicle force measured by the external balance and F_{prop} is the propeller force measured by the rotating shaft balance. The decomposition of forces is shown in Figure 8. Note that the drag of the spinner and hub assembly in propeller off configuration $D_{spin,iso}$ needs to be subtracted to asses the drag difference between propeller on and off conditions, as the force on the hub assembly and spinner are measured together with the propeller loads by the RSB. Hence, to asses the difference in drag upstream of the propeller, the hub assembly and spinner drag is subtracted. The magnitude of the hub assembly and spinner drag was determined with RANS CFD to approximately $C_{D,spin} \backslash C_{D,iso} \approx -0.12$. The force on the spinner and hub is acting in the thrust direction.

The drag polar of the isolated fuselage, including 95% confidence interval, is shown in Figure 9. The results show that there is a small asymmetry in the drag characteristics. With positive side-slip angles, the isolated fuselage drag is larger in comparison with the fuselage drag at negative angle of side-slip. Exploratory wake rake measurements have revealed a skewed wake as a result of an asymmetric vortical structure stemming from the fuselage-fairing junction. This is a limitation of the current setup and a deviation from the assumption of axisymmetric inflow conditions.

The installed performance of the propeller at various angles of side-slip beta is shown in Figure 10. Note that the angle of side-slip was varied in steps of $\Delta\beta = 2°$, but for clarity not all curves are presented. Although an analysis of the propeller performance with this boundary layer inflow is outside the scope of the current work, it is observed that the propeller thrust is sensitive to changes in angle of side-slip. To investigate the interaction of the propeller with the airframe, two different advance ratios have been selected: $J = 1.05$ and $J = 1.20$. These settings correspond to a thrust coefficient of $T_C = 0.56$ and $T_C = 0.33$ at $\beta = 0°$. For both settings, the propeller is operated on the flat part of the efficiency curve, thereby ensuring on-design conditions. Note that the conventional formulation of propeller efficiency,

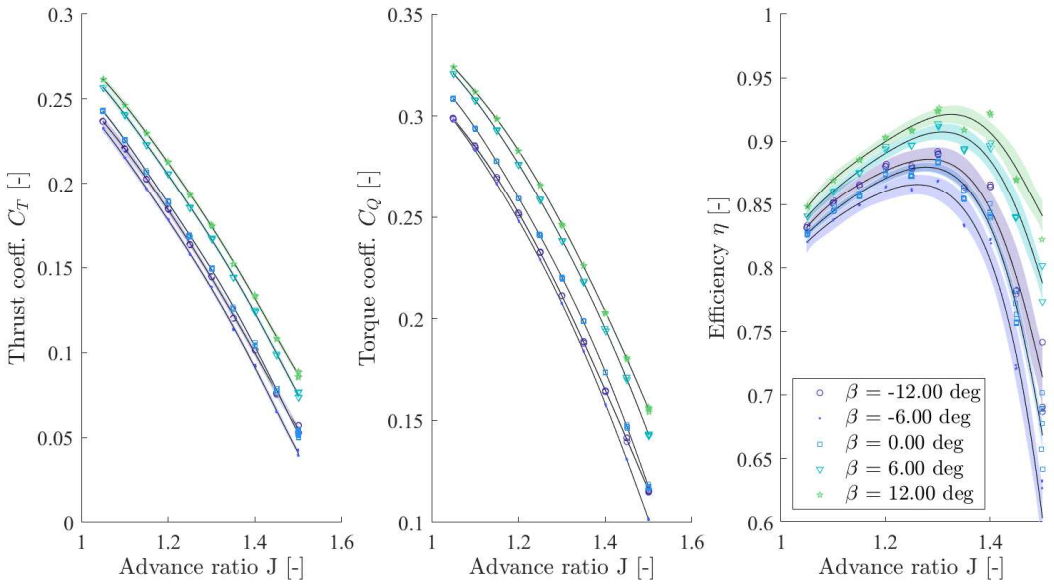

Fig. 10 Propeller performance curves for various angles of side-slip for $\beta_{0.70R} = 30°$. Original data with a 5^{th} order polynomial and 95% confidence interval.

$\eta = C_T \cdot J_\infty / C_P$, was used. In case of boundary layer ingestion, the scaling with the freestream velocity to express the efficiency is incorrect as it can result in non-physical (above unity) efficiency values [34]. However, as the efficiency is only used to demonstrate that the propeller was operating in a reasonable part of the performance envelope, this simplification was deemed acceptable.

At fixed relative speeds, the variation in thrust coefficient over the angle of side-slip range is $\Delta T_C \approx 0.06$ (Figure 11). Note that the errorbars represent a 95% confidence interval based on student-t distribution. The thrust coefficient is observed to vary with the side-slip angle. At positive side-slip angles, the thrust coefficient is larger in comparison to the case of zero-incidence. The variation in T_C with side-slip angle points at an asymmetry of inflow to the propeller, possibly stemming from the body-fairing interaction.

To obtain a better comprehension of the balance of forces, the normalized force of the propeller and fuselage are plotted in Figure 12 for $J = 1.05$. As shown, the excess thrust is several multitudes of the isolated fuselage drag. However, it should be noted that a wing and empennage are not included and that for most aircraft designs, $D_{fus} \approx 0.20 - 0.30 D_{tot}$. Furthermore, the drag of a more conventional fuselage ($FSR = L_{fus}/D_{fus} \approx 12.0$) will be approximately 1.4 larger based on ESDU predictions [28]. Hence, the observations are believed to be indicative for typical high-thrust conditions (e.g. takeoff). Nevertheless, in a quantitative sense, the results cannot directly be applied to aircraft designs utilizing BLI without additional considerations.

Using the isolated drag polar and the propeller thrust and side-force coefficients, the installed drag can be computed. This is presented in Figure 13, together with the drag of the isolated body. The drag due to propeller installation is

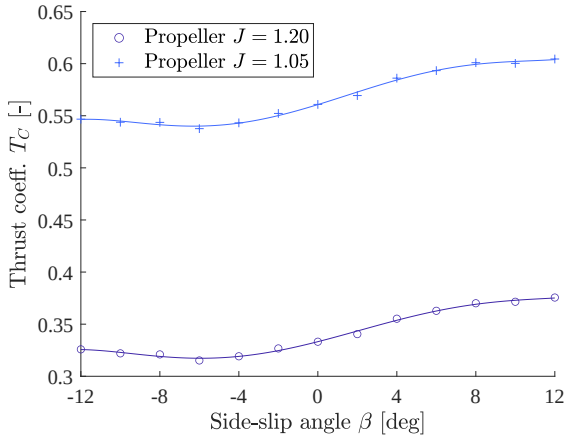

Fig. 11 Thrust coefficient T_C variation with angle of side-slip $\beta_{0.70R} = 30°$.

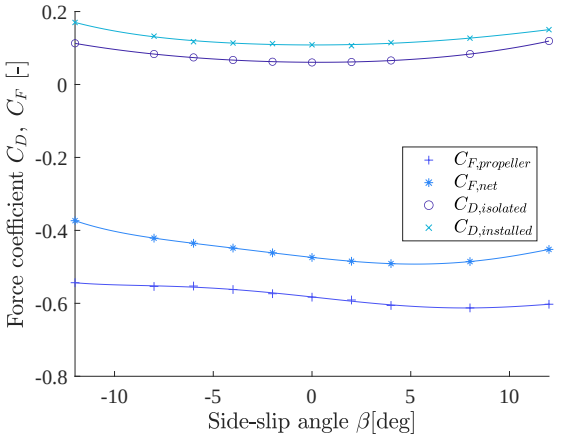

Fig. 12 Forces coefficients on the model with propeller for $J = 1.05$.

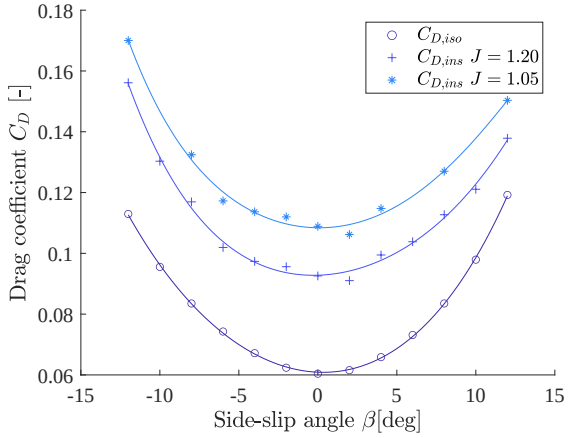

Fig. 13 Drag polars of the fuselage with installed propeller.

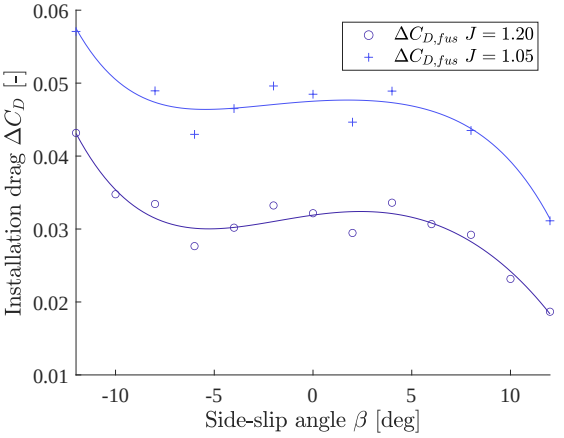

Fig. 14 Increment in fuselage drag ($\Delta C_{D,fus}$) as a result of propeller operation. $C_{D,iso} = 0.0604$.

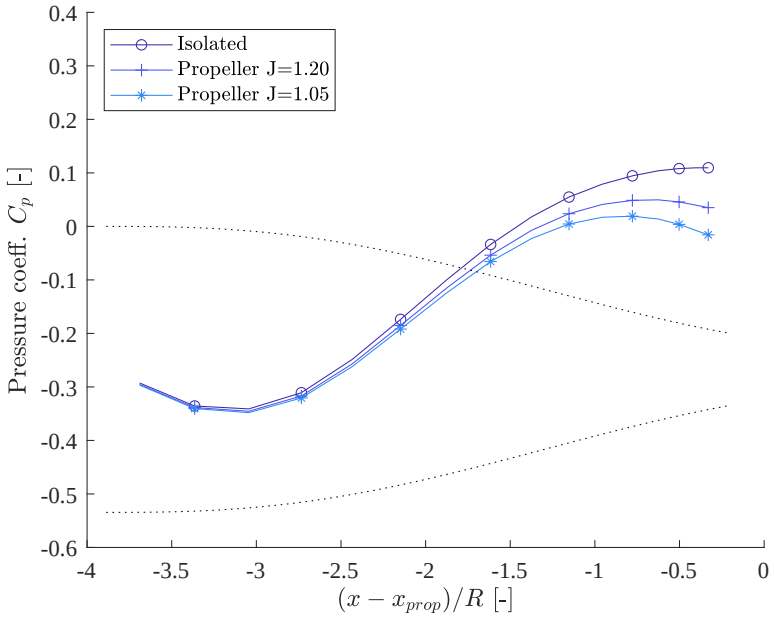

Fig. 15 Static pressure distribution on the fuselage body upstream of the propeller. Contour of the aftbody is added with dotted lines for reference.

obtained by subtraction of the isolated body drag from the installed drag. The results, provided in Figure 14, show that the drag increase is substantial since $C_{D,iso} = 0.0604$. As mentioned, the relatively large propeller size compared to the fuselage diameter and the low slenderness of the fuselage prohibit a direct translation of the result to more realistic aircraft designs. Nevertheless, it does highlight that the drag increase at higher thrust conditions due to the propeller can be substantial and needs to be taken into account. In the following part, the contribution of the pressure drag and viscous drag to the drag increase are discussed separately.

1. Pressure drag

The propeller-fuselage interference drag described in the previous section partially stems from a reduction of static pressure over the aftbody of the fuselage. To check the influence of the propeller on the pressure field, the pressure tap readings with and without the propeller were compared. The result is presented in Figure 15. The pressure gradient over the fuselage aftbody is altered due to propeller action from approximately $1D_p$ upstream of the propeller. At around $0.5D_p$ upstream, the induction by the propeller is large enough to change the sign of the pressure gradient, becoming favourable towards the propeller. As expected, the pressure gradient is strongly dependent on the thrust coefficient T_c. Another observation is that the pressure close to $2D_p$ upstream is almost unaffected by the propeller. The pressure distribution from Figure 15 was obtained from a single azimuthal position ($\theta = 90°$). To evaluate to what extent the flow field can be regarded as axisymmetric, readings at different azimuthal positions were obtained. The aftbody shells were rotated 360° with a 30° increment to obtain a pressure map consisting of 384 individual measurement points. The

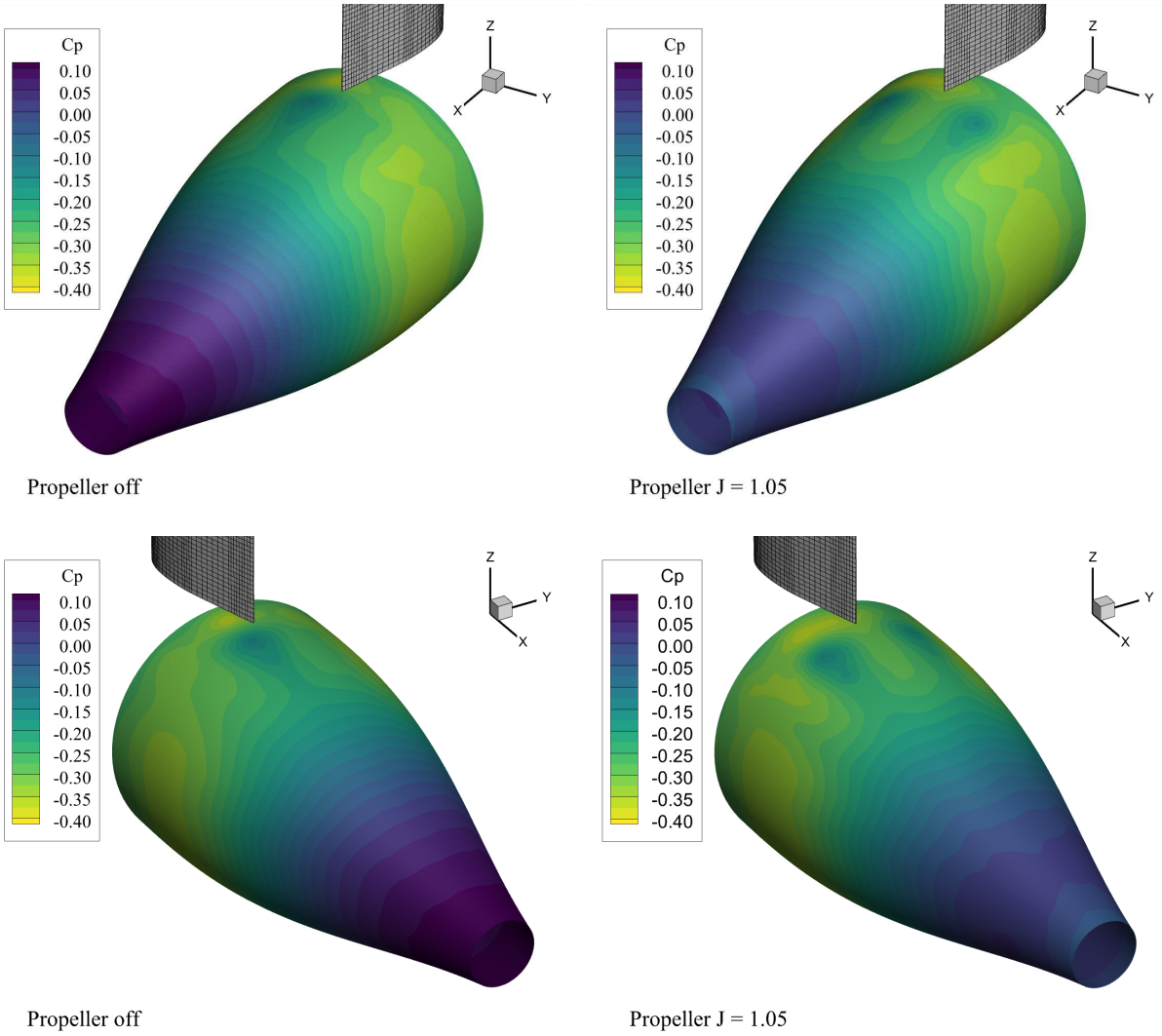

Fig. 16 Contours of pressure coefficient C_p for the isolated body and the propeller installed at $J = 1.05$ and $\beta = 0°$.

pressure ports of a single shell were used. Only in the case of the isolated body, the rotation of the shells was performed over 270° and for the remaining azimuthal positions, the pressure ports of the opposite shell were added. One of the rows of the opposite pressure shell featured erroneous readings, which was possibly due to an obstruction of one of the pressure tube bundles during the rotation. As such, for the isolated fuselage case, the ±45° around the vertical plane was sampled with a single pressure port row, reducing the number of pressure readings to 336. The data were interpolated to a refined grid using Kriging with a quadratic drift function [35]. Figure 16 compares the pressure distributions between the propeller-off and $J = 1.05$ cases, at $\beta = 0°$.

The pressure field can be regarded axisymmetric to a large extent, with the exception of the area ±45° of the support fairing. On both sides of the fairing, a patch of higher pressure is observed due to an interaction with the pressure field

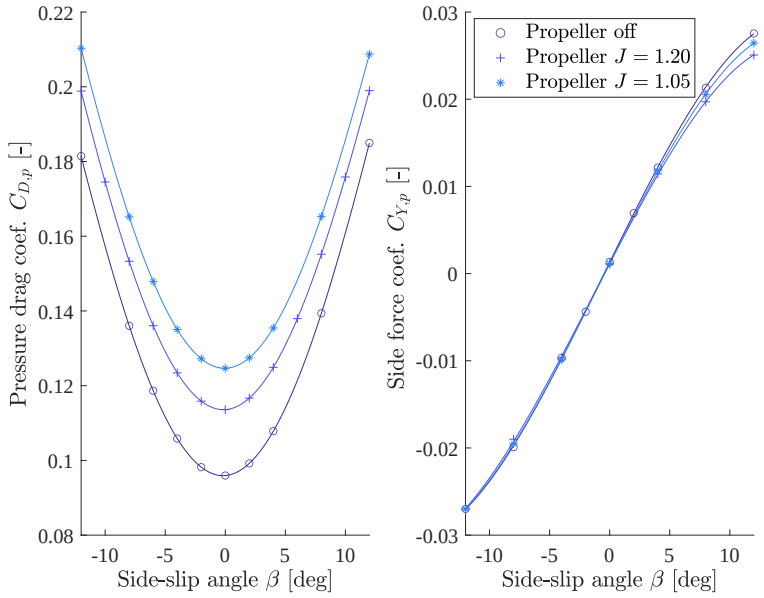

Fig. 17 Pressure force coefficients on the fuselage body upstream of the propeller. Pressure drag coefficient $C_{D,p}$ (left) and side force $C_{Y,p}$ (right).

of the fairing. Note that in the case of the isolated body, the resolution in this region is reduced, as discussed previously. As such, the effect of the support interference with the wall static pressure field is less detailed. Nevertheless, the contours show that the static pressure field at the beginning of the fuselage contraction is unaffected by the propeller throughout the circumference. Based on this observation, the assumption in the rest of the analysis is made that the drag from the fuselage nose to the mid-section is independent of the propeller operation and the variation in drag is predominantly caused by changes in the friction and pressure drag over the fuselage aftbody.

The pressure drag over the aftbody can be obtained by taking the surface integral of the pressure multiplied by the wall normal vector and then decomposing into wind axes. The result for the propeller-off and propeller-on cases are compared in Figure 17. In line with expectation, the change is predominately stemming from a difference in axial pressure force. As shown in the figure on the left, the pressure drag is increased by up to 30% in the case of $J = 1.05$ compared to the isolated configuration. In the case of $J = 1.20$, the relative difference is 21% at $\beta = 0°$. Note that the drag of the aftbody is larger than the total fuselage drag, which includes the force contribution of the nose cone acting in the opposite direction. On the left, the side force coefficient expressed in the body axis is presented. The side force is largely unaffected by the presence of the propeller. Small differences are observed only at larger, positive beta angles. However, the relative contribution of the side-force to the pressure drag term is small.

2. Friction drag

Having established the change in pressure drag due to propeller operation, the change in friction drag is investigated in this section. Since the change in pressure drag ($\Delta C_{D,p}$) for the aft fuselage was already obtained, the friction drag can be obtained indirectly by subtraction.

$$\Delta C_{D,f} = \Delta C_D - \Delta C_{D,p} \tag{2}$$

The breakdown of the interference drag, expressed relative to the isolated fuselage drag, is shown in Figure 18. The results show that the drag increase over the fuselage aftbody is substantial. At zero incidence angle ($\beta = 0°$), the additional total drag on the aft-fuselage is 65% and 90% of the total isolated fuselage drag for $J = 1.20$ and $J = 1.05$, respectively. Furthermore, a strong asymmetry is observed for the negative β angles. As shown in Figure 11, the thrust coefficient T_c drops towards the negative angle of incidence and vice versa. Exploratory wake rake measurements reveal a skewed wake as a result of an asymmetric vortical structure stemming from the body-fairing junction. In the case of negative β, an increased total pressure loss attributed to the spinner is observed together with a reduction of the average disc loading. Despite the strong influence of the body-fairing interaction at non-zero incidence angle, the analysis at zero incidence still provides useful insights. For example, the pressure drag is increased more than the friction drag when the propeller is operated at $J = 1.05$ compared to $J = 1.20$. At $J = 1.05$ the relative share of the friction and pressure drag to the overall drag increase is approximately equal. In contrast, at $J = 1.20$, the relative share of the friction drag (43% ΔC_D) is larger compared to the pressure drag (35% ΔC_D). Furthermore, the pressure drag penalty for the installation of the propeller is clearly at a maximum for zero incidence, as the body is aligned with the propeller stream tube.

In order to link the observed change in friction drag to the state of boundary layer, measurements were performed with a pitot-static tube that was traversed in the horizontal plane, in the direction normal to the local wall (see Figure 7). The boundary layer profile, expressed as $C_{p,t} = 1 + (P_{pitot} - P_{t,\infty})/Q_\infty$, is presented in Figure 19. The boundary layer extends radially to approximately $r/R \approx 0.56$ of the propeller. Although almost half of the blade is operating outside of the fuselage boundary layer, a substantial momentum deficit is still ingested by the propeller. As shown, the boundary layer thickness is reduced due to the reduction of the static pressure in case of the propeller operation. Furthermore, it is observed that the gradient of the total-pressure profile close to the wall is different between the three configurations. For the cases with the propeller, the gradient of the total pressure is larger, which is an indication of enhanced friction losses. Indeed, the total pressure closest to the wall is lowest in the case of the high thrust setting (T_c) corresponding to $J = 1.05$.

To obtain the velocity distribution of the boundary layer, measurements were conducted using a CTA hotwire boundary layer probe. The mean velocity profiles for the three cases under investigation are presented in Figure 20. The results

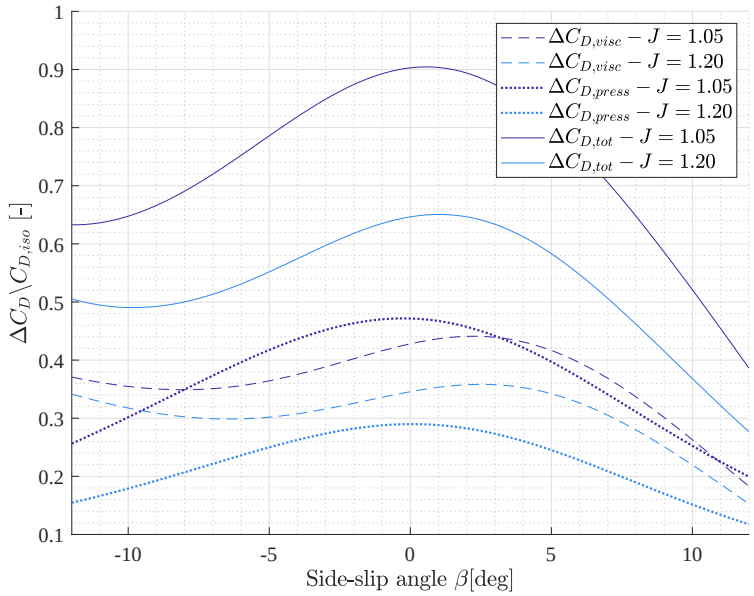

Fig. 18 Relative change in friction and pressure drag for cases with propeller compared with isolated body drag.

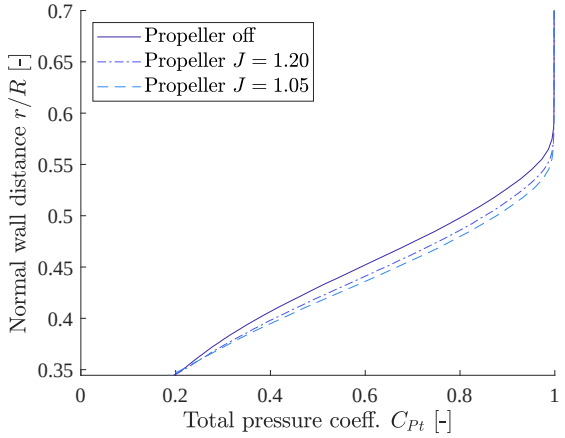

Fig. 19 Pitot-tube measurements of the boundary layer at $x/L_{fus} = 0.8840$ and $\beta = 0°$.

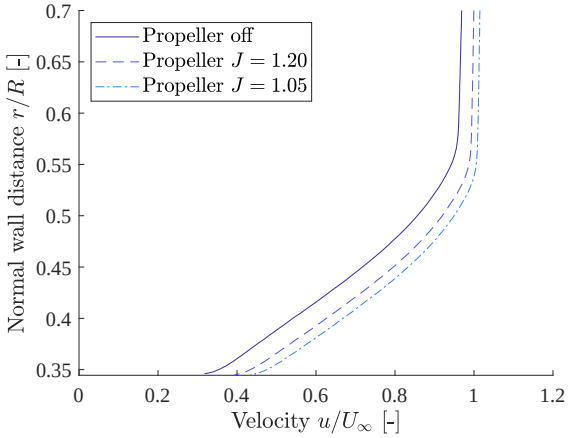

Fig. 20 Velocity profile of the boundary layer using CTA at $x/L_{fus} = 0.8840$ and $\beta = 0°$.

Table 2 Overview of boundary layer parameters for propeller-on and -off cases.

	Prop-off	Prop $J = 1.20$	Prop $J = 1.05$	
$\delta_{0.995}/R$	0.2326	0.2194	0.2130	[-]
δ^*	0.0128	0.0105	0.0096	m
θ	0.0071	0.0068	0.0066	m
H	1.79	1.55	1.45	[-]

show that the velocity profiles are similar in shape but are different in velocity magnitude. In the cases with the propeller, the velocity of the mean local flow is increased due to the contraction of the streamlines upstream of the propeller disc. As a result, the velocity gradient in the near wall region should be higher accordingly. In line with the previous observations made about the increased friction drag, this implies a higher local skin-friction coefficient.

To study the change in boundary layer characteristics further, the shape factor is calculated using trapezoidal integration of the measured profiles. The shape factor H is found to change from $H = 1.79$ for the isolated fuselage to $H = 1.55$ ($J = 1.20$) and $H = 1.45$ ($J = 1.05$) (Table 2). In order to interpret the differences between the profiles in a better way, the profiles are nondimensionalized with the boundary layer inner scales, as shown in Figure 21. The boundary layer profile for the isolated body was scaled by fitting the data to the log law ($\kappa = 0.41$, $B = 5.0$). This was performed in a gradient-based optimization loop where the fit error with a perfect log-law was minimized by introducing a correction on the wall distance. A correction on the wall distance of $\Delta y/\delta_{99} = 3.7e^{-3}$ was required to obtain a perfect fit. Considering the difficulty of probe alignment on a curved surface and the small displacements of the model under load, this is considered to be within the measurement uncertainty. The profiles for the propeller-on cases were scaled accordingly, using the same wall distance correction as for the isolated case. The profiles obtained with the propeller deviate from the log law, as the gradient in the log law region is less steep. This is in agreement with studies of strongly accelerated boundary layers [18]. A parameter for the study of boundary layers in accelerated flow conditions that is often used is the relative local acceleration, K, described by: [36]

$$K = \frac{\nu}{u^2}\frac{dU}{dx} \tag{3}$$

For the cases with the propeller, the acceleration constants were $K = 0.78e^{-6}$ and $K = 1.25e^{-6}$ for $J = 1.20$ and $J = 1.05$, respectively. Hence, both boundary layers are below the critical acceleration of $K = 3.5e^{-6}$ at which re-laminarization is found to occur. However, this criterion was obtained with experiments conducted at relatively low Reynolds number ($Re_\theta \leq 2{,}500$) [37]. For comparison, the Reynolds numbers in this work are $Re_\theta = 3.09e^4$ and $Re_\theta = 2.98e^4$ for $J = 1.20$ and $J = 1.05$, respectively. Nevertheless, the boundary layer at the current measurement location ($x/L = 0.8840$) can be considered to be in a laminarescent state [18] [38]. Considering that $u^+ = u\backslash u_\tau$, the difference in wall shear stress between the cases can be derived from the nondimensional velocity at the boundary-layer

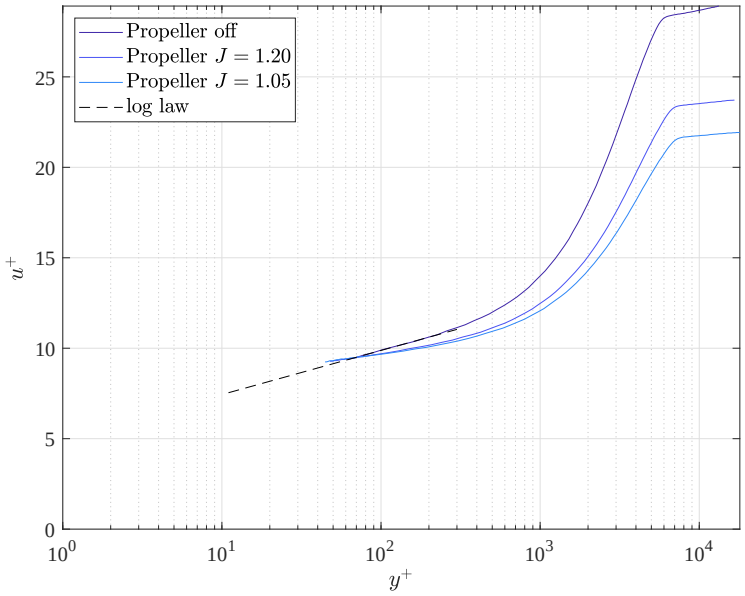

Fig. 21 Plot of nondimensional wall distance y^+ versus velocity u^+ in semi-logarithmic scale at $x/L_{fus} = 0.8840$ and $Re_L = 6.50e^6$.

edge. Acknowledging the fact that shear stress (τ_w) is estimated with the log-law fit and not based on direct measurement, the difference in local shear stress with respect to the isolated fuselage would be $\Delta\tau_w = 56\%$ and $\Delta\tau_w = 86\%$ for $J = 1.20$ and $J = 1.05$, respectively.

B. Unsteady propeller-fuselage interactions

In the previous section, the time-averaged interaction effects between the propeller and the fuselage aftbody were investigated. However, the unsteady interaction effects may be larger than the mean of the interactions. Hence, in this section, the unsteadiness of these interactions is investigated in more detail.

1. Velocity fluctuations

The mean velocity data from the hotwire measurements revealed a reduction of boundary layer thickness (δ_{99}) and shape factor (H) for the cases with operating propeller. Furthermore, it was demonstrated that the universal log-law is not valid for the accelerated boundary layer. The latter implies that the production and dissipation of turbulence are not in equilibrium. In order to investigate the turbulent properties of the boundary layer in more detail, the unsteadiness of the hotwire data is further investigated. The Power Spectral Density (PSD) of the velocity fluctuations in the boundary layer at two different wall-normal distances are provided in Figure 22. The frequency is expressed in terms of the Strouhal number:

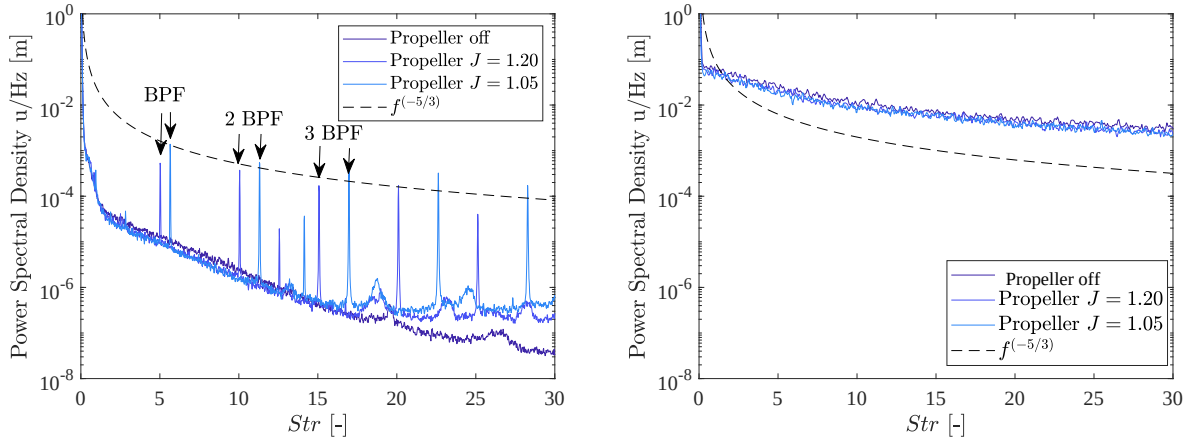

(a) $y = \delta_{99}$ **(b)** $y = 0.02 \cdot \delta_{99}$

Fig. 22 Power spectral density of u' at the inner and outer region of the boundary layer at $x/L_{fus} = 0.8840$.

$$Str = \frac{n \cdot D_p}{\bar{u}} \tag{4}$$

, where the propeller diameter (D_p) is used as a reference length scale and $\bar{u}$ the local mean velocity. The figure is capped at $Str = 30$ in order to better visualize the harmonics of the BPF. In Figure 22a, the PSD at the edge of the boundary layer $y = \delta_{99}$ is presented. The results show that the harmonics of Blade Passing Frequency (BPF) are clearly visible. Furthermore, up to $Str = 15$ there is a logarithmic decay of u' irrespective of the propeller. At higher frequencies, fluctuations remain at a higher level for the cases with propeller. In Figure 22b, the spectra are shown close to the wall, still within the log-law region. Submerged in the boundary layer, the level of u' is significantly higher and the peaks of the BPF harmonics are almost completely overshadowed by turbulence.

At high frequency, as shown in Figure 23, distinct peaks at $f = 7.5 \cdot f_{BPF}$ and its harmonics can be identified. The peaks at a non-integer multitude of the blade passing frequency were not observed in a previous test campaign. Furthermore, frequency analysis of the microphone data (Figure 28) does not reveal the same frequency peak. A possible cause could have been vibration of the support beam. Since no accelerometers were used, this hypothesis cannot be confirmed. Electronic interference with the power cables between the ESC and the BLDC could have been another source for this unexplained local peak. Nevertheless, the cause is not believed to be of aerodynamic origin and a bandstop filter was applied to filter these harmonics.

Besides the peaks at harmonics of the BPF, a distinct rise of the velocity fluctuations was observed at 14.8kHz. The source of this peak is believed to be electronic noise. To eliminate the noise elements from the spectrum, a bandstop filter of ±0.5 kHz was applied in the following analysis. To asses the decay of energy associated with the turbulence scales, a curve representing a $-5/3$ power law has also been added in Figures 22 and 23 [39]. As shown, the spectra

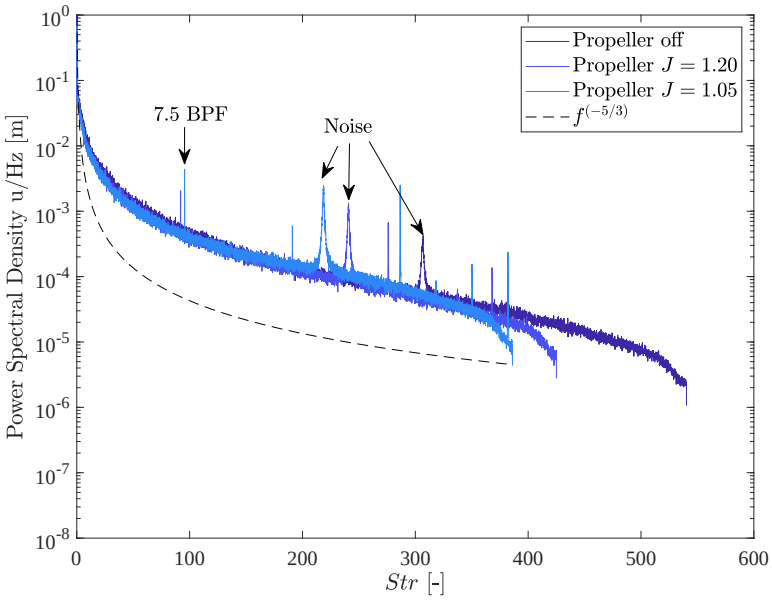

Fig. 23 Power spectral density of $u^{'}$ in the boundary layer near the wall ($y = 0.02 \cdot \delta_{99}$) at $x/L_{fus} = 0.8840$

follow the trend of the $-5/3$ power law. Since the rate of the decay in the energy spectrum is proportional to ϵ [40], this indicates that dissipation rate is not affected by the acceleration of the boundary layer. For the log-law region in a Zero Pressure Gradient (ZPG) turbulent boundary layer, the turbulence production (k) and dissipation (ϵ) are in equilibrium. For the accelerated boundary layer, the transport of turbulence from the friction sub-layer to the log-law region is disrupted, resulting in a growth of the friction sub-layer and a deviation from the universal log-law [18]. The deviation from the log-law has been demonstrated in Figure 21.

Although it was shown (Figure 22) that the peaks of f_{BPF} and its harmonics are overshadowed by the turbulence within the boundary layer, the periodic velocity fluctuations still persist. Using the one-per-revolution ($1p$) signal of the optical encoder, the measurement data were synchronized with the propeller rotation. A stroboscope was used to determine the phase delay between the trigger of the $1p$ signal and the reference blade passing the measurement location. Phase-locked averaging of the data ensures that only the response related to the periodic propeller blade passage is recorded, as the mean of the random fluctuations is zero. The result for $J = 1.05$ is shown in Figure 24. The results show that the passage of each individual blade is clearly visible. The dashed line indicates the passage of the reference blade. Within the boundary layer, the sudden rise in velocity is followed by a reduction after the blade passage (Figure 24c). This is in accordance with earlier observations [21]. At the boundary layer edge (Figure 24b) and outside the boundary layer (Figure 24a), the drop in velocity after the blade passage is not observed. Interestingly, the magnitude of the velocity perturbations does not change significantly whether inside or outside of the boundary layer. In contrast, the width of the perturbations measured outside of the boundary layer are noticeably wider. This effect is believed to be

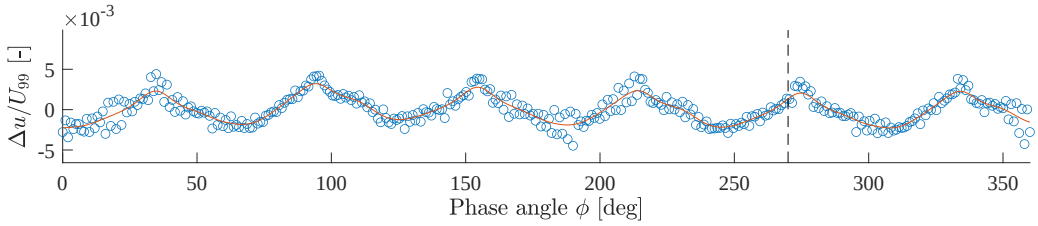

(a) $r/R = 0.80$ $\delta_{99}/R = 1.38$**.**

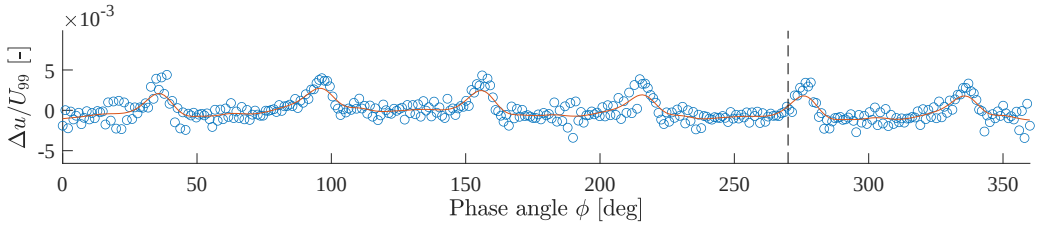

(b) $r/R = 0.58$ **or** $\delta_{99}/R = 1.00$**.**

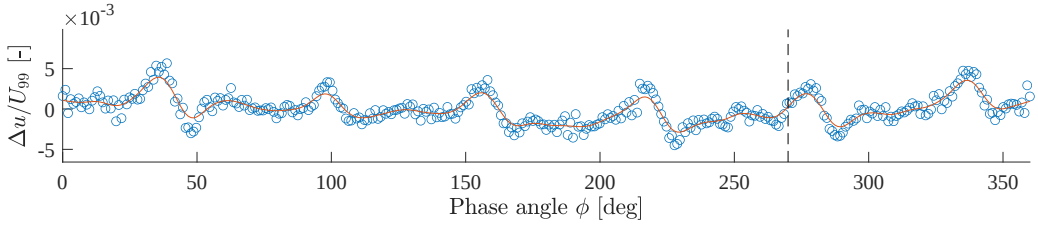

(c) $r/R = 0.3489$ **or** $\delta_{99}/R = 0.02$**.**

Fig. 24 Phase-locked velocity perturbations upstream of the propeller for $J = 1.05$ **at** $x/L_{fus} = 0.8840$**.**

directly dependent on the blade geometry and loading distribution. In terms of displacement effect, the TUD-XPROP has an almost constant chord and thickness distribution in the lower sections, but features an increase in chord from the mid-section towards the tip. Nevertheless, it is observed that the magnitude of the velocity perturbations coupled to the propeller blade passage are small at $\Delta u/U_\infty \approx 0.5\%$. When expressed in terms of advance ratio ($\Delta J \leq 0.01$), the perturbations are not expected to affect the mean propeller performance. Furthermore, the mean state of the boundary layer (e.g. H) is not expected to be altered by the propeller induced perturbations. Nevertheless, the perturbations could play an important role in the production of tonal and structure-born noise.

Besides the propeller-induced perturbations, it was shown in Figure 22 that the energy density of the velocity fluctuations increases significantly between the outer (Figure 22a) and inner region (Figure 22b) of the boundary layer. To investigate the distribution of turbulence throughout the boundary layer, profiles of turbulence intensity (I_x) are presented in Figure 25. It is observed that outside of the boundary layer, the axial turbulence intensity is relatively low; $I_x < 0.5\%$ for all cases. At the edge of the boundary layer, the turbulence intensity increases rapidly to at least one order of magnitude larger than the flow outside of the boundary layer. The maximum turbulence intensity is reached at around $r/\delta_{99} \approx 0.30$ ($y^+ \sim 1000$). For the cases with the propeller, the peak of turbulence intensity is lower compared to that observed for the isolated fuselage. In contrast, the level of the turbulence intensity near the wall is highest for the case of $J = 1.05$.

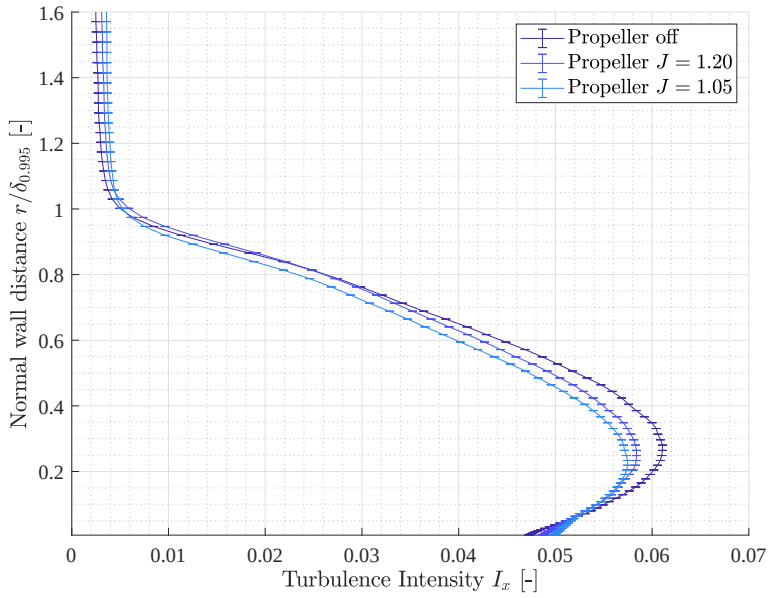

Fig. 25 Profiles of turbulence intensity throughout the boundary layer with 95% confidence interval.

These observations support the hypothesis that the rate of transport of turbulence from the inner region to the outer region of the boundary layer is reduced when the boundary layer is strongly accelerated [38].

2. Surface pressure fluctuations

Although the time-dependent velocity near the wall was obtained with the hotwire, the friction sub-layer and buffer region could not be probed. In order to get more insight in the fluctuations at the wall, microphones were used. With the microphones, both the hydrodynamic and acoustic pressure data were measured simultaneously. In conjunction with the velocity data stemming from the hotwire, the data can still provide insight into the turbulence levels at the wall. Similar to the static pressure ports, the microphones were rotated together with the aftbody to obtain a complete azimuthal map of the pressure fluctuations over the fuselage aftbody. The azimuthal resolution was $\Delta\theta = 30°$. Contours of the SPL are shown in Figure 26.

Note that the data of microphones 5, 7 and 9 were excluded from the analysis, as these were showing a consistent erroneous output. In order to smooth the contours, the Kriging interpolation was relaxed by introducing a non-zero range, 0.3 for the invariance, and a normalized semi-variance of 0.4. Shown on the left is the broadband noise contribution. A bandpass filter was applied from 50 Hz to 5 kHz and the harmonics of BPF have been removed with a bandstop filter. On the right, the SPL of the tonal content at the BPF and its harmonics is presented separately. The results show that there is a distinct zone with elevated levels of broadband noise behind the fairing. Comparing between the different configurations, it is observed that the levels of the broadband pressure fluctuations increase when the propeller

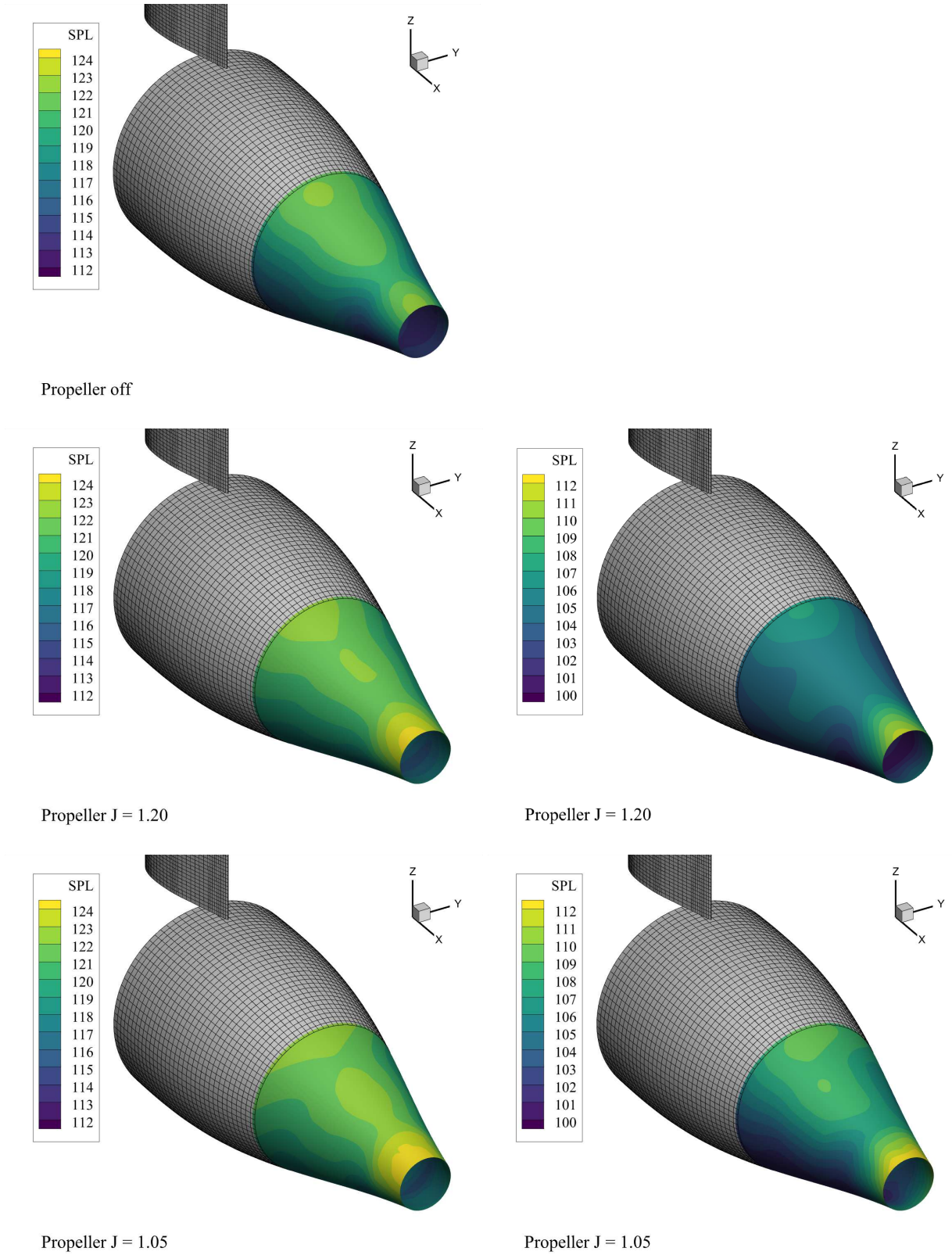

Fig. 26 Contours of broadband noise up to 5 kHz (left) and the tonal noise (right) over the aft-fuselage at $\beta = 0°$.

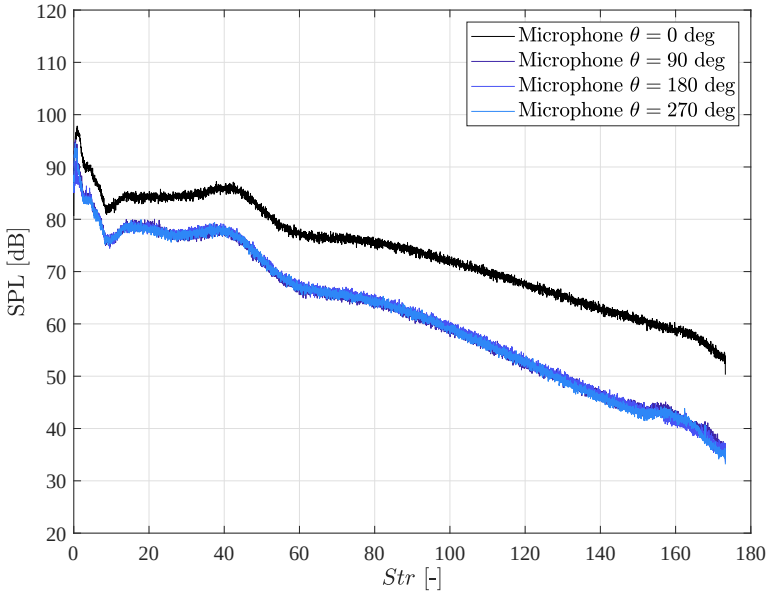

Fig. 27 Spectral densities for the isolated fuselage at various azimuthal positions; $\beta = 0°$, $x/L = 0.8840$.

is operated and thrust coefficient increased. This can be partially explained by the fact that the propeller, aside from tonal noise, also generates broadband noise (e.g. trailing edge). However, analysis of the turbulence intensity (Figure 25) showed that the very near wall turbulence levels are enhanced in the case when the propeller is operating, despite a reduction of turbulence levels further away from the wall. Next to the broadband noise, the tonal noise in the region behind the fairing are observed to be significantly higher compared to the rest of the aftbody. When a propeller blade encounters the wake of the fairing, the blade loading temporarily increase as a result of increased local blade angle of attack. The largest pressure fluctuations are found in the near-hub region. Compared to the broadband contours, the tonal noise appears to be more confined to the fairing wake region.

To investigate the change in pressure fluctuations in azimuthal direction, the spectral density of $p^{'}$ at four different azimuthal positions are shown in Figure 27 for the case of the isolated fuselage. The rsults show that the spectra for $\theta = 90°$ and $\theta = 180°$ are nearly identical. However, the spectrum at $\theta = 0°$ shows consistently higher levels of fluctuations. This is in accordance with the observation from the SPL contours (Figure 26). Furthermore, it demonstrates the pressure fluctuations in the sector $90° \leq \theta \leq 270°$ are not significantly affected by the model support wake. This observation confirms that the assumption of axisymmetric flow in the $\theta = 270°$ horizontal plane for the hotwire measurement was valid.

To understand the effect of the periodic blade passage on the SPL, the spectral density, with the frequency normalized by the blade passing frequency, is shown in Figure 28. For comparison, the spectrum for the isolated fuselage normalized by f_{BPF} of $J = 1.20$ is also shown. At f_{BPF}, a distinct peak of $\Delta SPL \approx 17$ dB can be observed. This in agreement

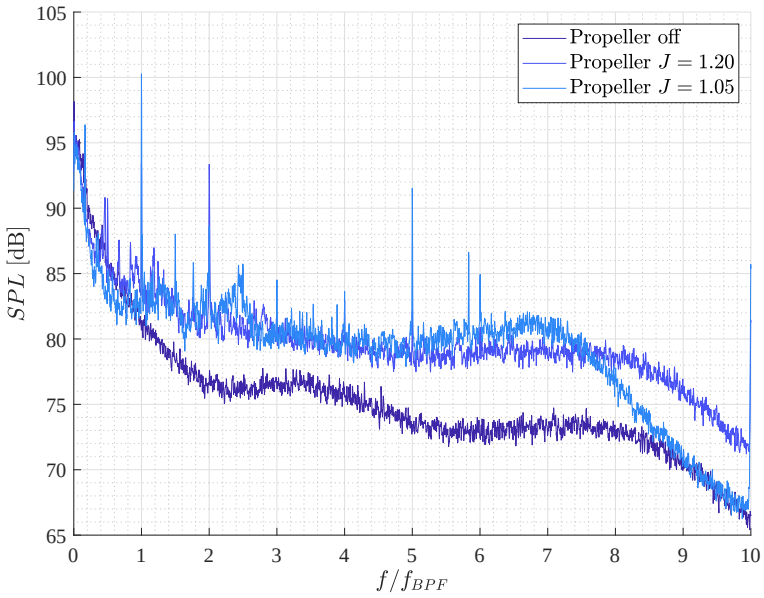

Fig. 28 Spectral densities versus the Blade Passing Frequency (BPF) at $\beta = 0°$, measured at $\theta = 270°$ and $x/L = 0.8840$.

with the observations in Figure 26. Up to six harmonics of the BPF can be identified. The $4th$ harmonic ($f/f_{BPF} = 5$) is significantly higher and approximately of the same level as of the $1st$ ($f/f_{BPF} = 2$). The reason for this is believed to be electronic interference with the electric motor, which features 30 poles. The number of poles coincides with the frequency of the observed peaks. Interestingly, there are also two peaks at $1.5 f_{BPF}$ and $2.5 f_{BPF}$ in the case of $J = 1.05$. However, in the case of $J = 1.20$, this was not observed. The root cause of this was not established and for further analysis, the frequency was filtered out.

To investigate the pressure fluctuations associated with the BPF in more detail, phase-locked averaging of band-filtered microphone data was performed. This is shown in Figure 29a for $J = 1.20$. The results show that there are clear pressure fluctuations at each blade passage. At $\theta = 270°$, the magnitude of the pressure fluctuations is $\Delta p \approx 5$ Pa. For comparison, the result for $J = 1.05$ is also presented in Figure 29b. A distinct difference is that the pressure fluctuations are almost doubled compared to $J = 1.20$. As such, it can be concluded that the pressure fluctuations, in accordance with expectation, scale approximately quadratically with T_c. Furthermore, it is observed that the fluctuations are not a clear single peak-per-blade passage, but consist of a main peak followed by several secondary peaks. Since the pressure fluctuations consist of both hydrodynamic and acoustic fluctuations, the secondary peaks could stem from either the propeller or a different acoustic source (e.g. drive train). Since the phase-locked hotwire data (Figure 24c) do not show the secondary peaks, it is believed that the additional in-phase fluctuations stem from a mechanical noise source. To add to this, the phase-locked p' values for $\theta = 0°$ and $J = 1.20$ are shown in Figure 29c. As shown, the peaks in the plane of the fairing have doubled in magnitude, corresponding to the observations from Figure 26. Hence, this reconfirms that a

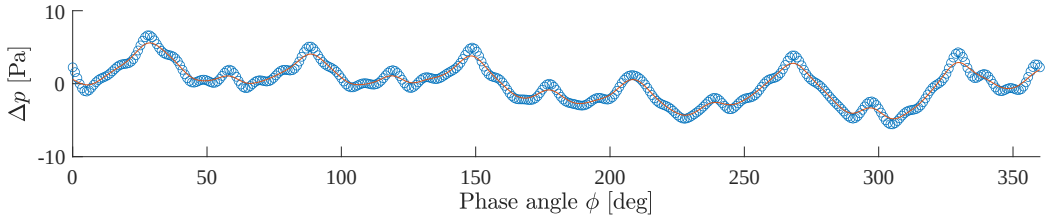

(a) $\theta = 270°$ **for** $J = 1.20$

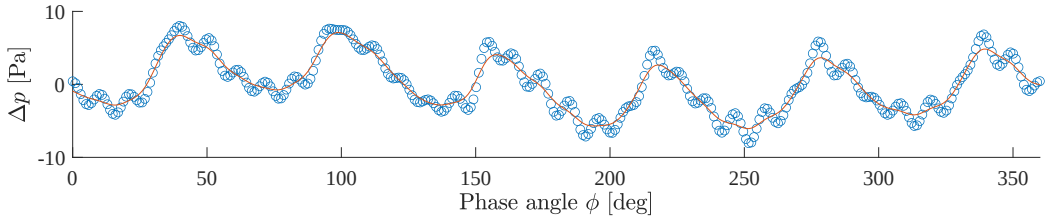

(b) $\theta = 270°$ **for** $J = 1.05$

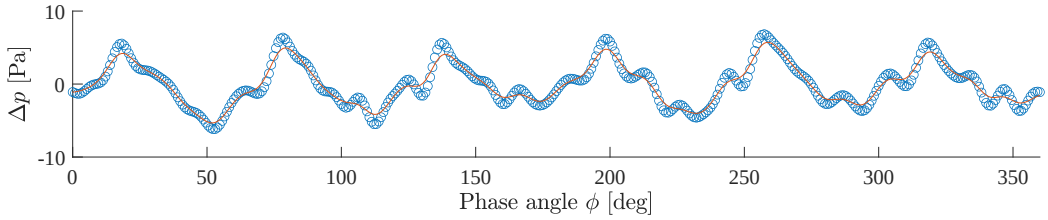

(c) $\theta = 0°$ **for** $J = 1.20$

Fig. 29 Phase-locked pressure perturbations at different azimuthal positions and thrust levels.

narrow wake encounter by the propeller should be avoided if possible, to reduce noise emissions.

IV. Conclusion

In this paper, the steady and unsteady effects of a aft-cone mounted propeller on the aerodynamic properties of a fuselage aft-body are presented. A subsonic wind tunnel experiment was conducted at the Delft University of Technology's Low Turbulence Tunnel (LTT) with a low slenderness ratio fuselage model. As a novelty, the forces acting on a propeller operating in the boundary layer of an axisymmetric fuselage model were reported. Together with the net force acting on the model, extensive surface pressure measurements were utilized to determine the effect of propeller installation on the fuselage friction and pressure drag. It was demonstrated that the aft fuselage pressure drag is increased by up to 30% at thrust conditions representative of takeoff conditions ($T_c = 0.56$). In conjunction, the friction drag was reported to contribute up to 43% of the total drag increase. The static pressure distribution over the aft fuselage shows reversal of the adverse pressure gradient within $0.5D_p$ upstream of the propeller compared to the isolated fuselage. The corresponding acceleration constants were $K = 0.76e^{-6}$ and $K = 1.25e^{-6}$ for $J = 1.20$ and $J = 1.05$, respectively. Measurements of the boundary layer upstream of the propeller revealed that the boundary layer is, in both cases, in a laminarescent state and thus, features significantly different characteristics than the fully-turbulent boundary layer on

the baseline fuselage without propeller effect. The boundary layer shape factor was reduced from $H = 1.79$ for the isolated fuselage to $H = 1.45$ with the propeller operating at $J = 1.05$. It was demonstrated that the nondimensional profiles of the cases with the propeller do not conform to the universal log-law of a zero pressure gradient turbulent boundary layer. Instead, the slope of the log-law region is considerably lower. Hotwire CTA indicates that operating the propeller increases the turbulence intensity near the wall noticeably. Locally, an increase of the skin friction of up to 85% was found. These findings suggest that the increase in viscous drag ahead of the propeller is not only caused by induced velocity by the propeller, but also due to an increased level of wall bounded turbulence as a result of boundary layer acceleration. In addition, perturbations of the velocity in phase with the propeller blade passage were observed. These perturbations were found to be persistent throughout the boundary layer. The magnitude of the perturbations was found to be small ($u'/U_{inf} \leq 0.5\%$) and did not scale linearly with T_c. Although the observed perturbations could be an important factor for noise emissions, the fluctuations do not change the mean characteristics of the boundary layer inflow to the propeller and, thereby, it was concluded that they do not have a significant impact on the time-averaged performance of the configuration. Embedded microphone measurements were taken to study the unsteady pressure field over the fuselage aftbody. The measurements revealed pressure fluctuations in phase with the propeller blade passage. Overall, the presented data show that the boundary layer ahead of a BLI propeller does not have significant transient response and that the time-averaged performance of the configuration can be modelled with steady-state models (e.g. RANS). However, it is shown that these models should account for the change in turbulence characteristics as a result of the boundary layer acceleration. Furthermore, the unsteady velocity and pressure measurements could attribute to further study of the acoustic properties of a fuselage BLI configuration with an open rotor.

Acknowledgments

This work was conducted within the Advanced Propulsion and Power Unit (APPU) project, which has received funding from the Dutch Ministry of Economic Affairs and Climate under the TKI scheme (Grant number TKI HTSM/18.0170) along with SAFRAN Tech. The authors would like to thank Peter den Dulk, Rob van der List and Ed Roessen of DEMO for manufacturing of the wind tunnel model and providing technical support during the design of the model. In addition, the authors would like to thank Biagio Della Corte for his assistance in the preparation and execution of the test campaigns. The authors are grateful also for the support received by the wind tunnel technicians, Emiel Langedijk and Stefan Bernardy.

References

[1] European Commission, Directorate-General for Mobility and Transport, and Directorate-General for Research and Innovation, *Flightpath 2050 – Europe's vision for aviation*, Publications Office, 2011. https://data.europa.eu/doi/10.2777/50266.

[2] *Strategic Research and Innovation Agenda*, ACARE, 2011. https://www.clean-aviation.eu/sites/default/files/

2022-01/CAJU-GB-2021-12-16-SRIA_en.pdf.

[3] *ICAO Environmental Report 2019*, ICA, 2019, Chap. Environmental Trends in Aviation to 2050.

[4] Gössling, S., and Humpe, A., "The global scale, distribution and growth of aviation: Implications for climate change," *Global Environmental Change*, Vol. 65, 2020, p. 102194. https://doi.org/10.1016/j.gloenvcha.2020.102194.

[5] Grewe, V., Rao, A. G., Gronstedt, T., and et al., "Evaluating the climate impact of aviation emission scenarios towards the Paris agreement including COVID-19 effects," *Nature Communications*, 2021. https://doi.org/10.1038/s41467-021-24091-y.

[6] Hall, D. K., Huang, A. C., Uranga, A., Greitzer, E. M., Drela, M., and Sato, S., "Boundary Layer Ingestion Propulsion Benefit for Transport Aircraft," *Journal of Propulsion and Power*, Vol. 33, No. 5, 2017, pp. 1118–1129. https://doi.org/10.2514/1.B36321.

[7] Yildirim, A., Gray, J. S., Mader, C. A., and Martins, J. R. R. A., "Boundary-Layer Ingestion Benefit for the STARC-ABL Concept," *Journal of Aircraft*, Vol. 59, No. 4, 2022, pp. 896–911. https://doi.org/10.2514/1.C036103.

[8] Seitz, A., Habermann, A. L., Peter, F., Troeltsch, F., Castillo Pardo, A., Della Corte, B., van Sluis, M., Goraj, Z., Kowalski, M., Zhao, X., Grönstedt, T., Bijewitz, J., and Wortmann, G., "Proof of Concept Study for Fuselage Boundary Layer Ingesting Propulsion," *Aerospace*, Vol. 8, No. 1, 2021. https://doi.org/10.3390/aerospace8010016.

[9] Giannakakis, P., Maldonado, Y.-B., Tantot, N., Frantz, C., and Belleville, M., "Fuel Burn Evaluation of a Turbo-Electric Propulsive Fuselage Aircraft," *AIAA Propulsion and Energy Forum*, 2019. https://doi.org/10.2514/6.2019-4181.

[10] Steiner, H.-J., Seitz, A., Wieczorek, K., Plötner, K., Isikveren, A. T., and Hornung, M., "Multi-disciplinary design and feasibility study of distributed propulsion systems," *28th International Congress of the Aeronautical Sciences*, 2012, pp. 23–28.

[11] Habermann, A. L., Bijewitz, J., Seitz, A., and Hornung, M., "Performance bookkeeping for aircraft configurations with fuselage wake-filling propulsion integration," *CEAS Aeronautical Journal*, Vol. 11, 2020, pp. 529–551. https://doi.org/10.1007/s13272-019-00434-w.

[12] Drela, M., "Power Balance in Aerodynamic Flows," *AIAA Journal*, Vol. 47, No. 7, 2009, pp. 1761–1771. https://doi.org/10.2514/1.42409.

[13] Arntz, A., Atinault, O., and Merlen, A., "Exergy-Based Formulation for Aircraft Aeropropulsive Performance Assessment: Theoretical Development," *AIAA Journal*, Vol. 53, No. 6, 2015, pp. 1627–1639. https://doi.org/10.2514/1.J053467.

[14] Hickling, C., Balantrapu, N. A., Alexander, W. N., Millican, A. J., Devenport, W. J., and Glegg, S. A., "Turbulence Ingestion into a Rotor at the Rear of an Axisymmetric Body," *25th AIAA CEAS Aeroacoustics Conference*, 2019. https://doi.org/10.2514/6.2019-2571.

[15] Zhou, D., Wang, K., and Wang, M., "Computation of Rotor Noise Generation in a Thick Axisymmetric Turbulent Boundary Layer," *AIAA AVIATION FORUM*, 2021. https://doi.org/10.2514/6.2021-2186.

[16] Schatzman, D. M., and Thomas, F. O., "An Experimental Investigation of an Unsteady Adverse Pressure Gradient Turbulent Boundary Layer: Embedded Shear Layer Scaling," *Journal of Fluid Mechanics*, Vol. 815, 2017, p. 592–642. https://doi.org/10.1017/jfm.2017.65.

[17] Nishioka, M., and Morkovin, M. V., "Boundary-layer receptivity to unsteady pressure gradients: experiments and overview," *Journal of Fluid Mechanics*, Vol. 171, 1986, p. 219–261. https://doi.org/10.1017/S002211208600143X.

[18] Bourassa, C., and Thomas, F., "An experimental investigation of a highly accelerated turbulent boundary layer," *Journal of Fluid Mechanics*, Vol. 634, 2009, pp. 359–404. https://doi.org/10.1017/S0022112009007289.

[19] Sinnige, T., Ragni, D., and Malgoezar, A. e. a., "APIAN-INF: an aerodynamic and aeroacoustic investigation of pylon-interaction effects for pusher propellers," *CEAS Aeronautical Journal*, Vol. 9, 2018, pp. 291–306. https://doi.org/10.1007/s13272-017-0247-2.

[20] Sandahl, C. A., *Wind-tunnel investigation of effects of a pusher propeller on lift, profile drag, pressure distribution, and boundary-layer transition of a flapped wing*, National Advisory Committee for Aeronautics, 1945.

[21] Barlett, W., and Marino, A., "An investigation on mutual interferrrence effects of a tail surface - stern propeller installation on a model simulating the Douglas XB-42 empennage," Wartime report, NACA, 1944.

[22] Liu, X., and Marshall, J. S., "Blade penetration into a vortex core with and without axial core flow," *Journal of Fluid Mechanics*, Vol. 519, 2004, p. 81–103. https://doi.org/10.1017/S0022112004001302.

[23] Yang, Y., Veldhuis, L., and Eitelberg, G., "Aerodynamic impact of a streamwise vortex on a propeller," *Aerospace Science and Technology*, Vol. 70, 2017, pp. 108–120. https://doi.org/10.1016/j.ast.2017.08.004.

[24] Zehner, P., Falissard, F., and Gloerfelt, X., "Vortex Model and Blade Span Influence on Orthogonal Blade-Vortex Interaction Noise," *AIAA Journal*, Vol. 58, No. 8, 2020, pp. 3405–3413. https://doi.org/10.2514/1.J058878.

[25] Moffit, B., "Analysis and Testing of Boundary-Layer-Ingesting Pusher Propeller for High Speed Rotorcraft," *AHS international 73rd Annual Forum & Technology Display*, 2017, pp. 649–661. https://doi.org/10.4050/F-0073-2017-12012.

[26] Serpieri, J., "Cross-Flow Instability: Flow diagnostics and control of swept wing boundary layers," Dissertation, Delft University of Technology, 2018. https://doi.org/10.4233/uuid:3dac1e78-fcc3-437f-9579-048b74439f55.

[27] Della Corte, B., Perpignan, A. A., van Sluis, M., and Rao, A. G., "Experimental and Computational Analysis of Model–Support Interference in Low-Speed Wind-Tunnel Testing of Fuselage-Boundary-Layer Ingestion," *9th EASN International Conference*, 2019. https://doi.org/10.1051/matecconf/201930402020.

[28] Chappell, P., Clarke, A., R.Porter, and Wood, S., "Geometrical Characteristics of Typical Bodies," Tech. rep., IHS ESDU, 1977.

[29] Mcmasters, J. H., and Henderson, M. L., "Low-speed single-element airfoil synthesis," *Technical Soaring*, Vol. 6, 1979, pp. 1–21.

[30] Rengasamy, K., and Mandal, A. C., "Experiments on effective tripping device in a zero pressure gradient turbulent boundary layer," *Journal of Physics: Conference Series*, Vol. 822, No. 1, 2017. https://doi.org/10.1088/1742-6596/822/1/012016.

[31] Stokkermans, T. C. A., and Veldhuis, L. L. M., "Propeller Performance at Large Angle of Attack Applicable to Compound Helicopters," *AIAA Journal*, Vol. 59, No. 6, 2021, pp. 2183–2199. https://doi.org/10.2514/1.J059509.

[32] Li, Q., Öztürk, K., Sinnige, T., Ragni, D., Eitelberg, G., Veldhuis, L., and Wang, Y., "Design and Experimental Validation of Swirl-Recovery Vanes for Propeller Propulsion Systems," *AIAA Journal*, Vol. 56, No. 12, 2018, pp. 4719–4729. https://doi.org/10.2514/1.J057113.

[33] Turan, O., Azad, R., and Atamanchuk, T. M., "Wall effect on the hot-wire signal without flow," *Journal of Physics E: Scientific Instruments*, Vol. 20, No. 10, 1987, p. 1278. https://doi.org/10.1088/0022-3735/20/10/028.

[34] Smith, L. H., "Wake ingestion propulsion benefit," *Journal of Propulsion and Power*, Vol. 9, No. 1, 1993, pp. 74–82. https://doi.org/10.2514/3.11487.

[35] Davis, J., *Statistics and Data Analysis in Geology*, Wiley, 1986.

[36] Launder, B. E., "Laminarization of the Turbulent Boundary Layer in a Severe Acceleration," Ph.D. thesis, Massachusetts Institute of Technology, 1965. https://doi.org/10.1115/1.3629738.

[37] Sreenivasan, K., "Laminarescent, relaminarizing and retransitional flows," *Acta Mechanica*, Vol. 44, 1982, pp. 1–48. https://doi.org/10.1007/BF01190916.

[38] Fernholz, H. H., and Warnack, D., "The effects of a favourable pressure gradient and of the Reynolds number on an incompressible axisymmetric turbulent boundary layer. Part 1. The turbulent boundary layer," *Journal of Fluid Mechanics*, Vol. 359, 1998, p. 329–356. https://doi.org/10.1017/S0022112097008513.

[39] Kolmogorov, A. N., "The local structure of turbulence in incompressible viscous fluid for very large Reynolds," *Numbers. In Dokl. Akad. Nauk SSSR*, Vol. 30, 1941, p. 301. https://doi.org/10.1098/rspa.1991.0075.

[40] Schröder, M., Bätge, T., Bodenschatz, E., Wilczek, M., and Bagheri, G., "Estimating the turbulent kinetic energy dissipation rate from one-dimensional velocity measurements in time," *Atmospheric Measurement Techniques Discussions*, Vol. 2023, 2023, pp. 1–45. https://doi.org/10.5194/amt-2023-63.